

Assessing the relative importance of methane super-emitters and diffuse area sources in quantifying total emissions for oil and gas production areas in Algeria

S. Naus^{1,*}, J. D. Maasakkers¹, R. Gautam², M. Omara², R. Stikker¹, A. K. Veenstra¹, B. Nathan¹, I. Irakulis-Loitxate^{3,4}, L. Guanter^{2,3}, S. Pandey^{1,5}, M. Girard⁶, A. Lorente-Delgado^{1,2}, T. Borsdorff¹, and I. Aben¹

¹SRON Netherlands Institute for Space Research, Leiden, Netherlands

²Environmental Defense Fund, Washington, DC 20009, USA

³Research Institute of Water and Environmental Engineering (IIAMA), Universitat Politècnica de València (UPV), Valencia 46022, Spain

⁴International Methane Emission Observatory, United Nations Environment Program, Paris, France

⁵Jet Propulsion Laboratory, California Institute of Technology, Pasadena, CA, US

⁶GHGSat Inc, Montréal, Canada

*Corresponding author: Stijn Naus (stijn.naus@niwa.co.nz)

June 17, 2023

This version of the manuscript is a preprint, and has not yet undergone peer review. Therefore, the content of this article is still subject to change. Please feel free to contact the corresponding author; we welcome feedback.

Abstract

Methane emissions from oil and gas production provide an important and partly mitigable contribution to anthropogenic global warming. Here, we investigate 2020 emissions from the largest gas field in Algeria, Hassi R'Mel, and the oil production dominated area of Hassi Messaoud. We first use methane data from the high-resolution (20 m) Sentinel-2 instrument to identify eleven point source super-emitters (1 in Hassi R'Mel and 10 in Hassi Messaoud), ten of which correspond to unlit flares likely related to oil production. For each point source we construct emission timeseries based on methane enhancements as observed with Sentinel-2. We integrate this information in a transport model inversion that uses methane data from the coarser ($7.5 \times 5\text{km}^2$) but higher-precision TROPOMI instrument to estimate emissions from both diffuse area sources and the 11 super-emitting point sources (> 1 t/hr individually). Compared to the bottom-up inventory of Scarpelli et al. [2022] for 2019 that is aligned with UNFCCC-reported emissions, we find that 2020 emissions in Hassi R'Mel (0.16 [0.11-0.22] Tg/yr) are lower by 53 [24-73]%, and emissions in Hassi Messaoud (0.22 [0.13-0.28] Tg/yr) are higher by 79 [4-188]%. Both the Sentinel-2 analysis and the TROPOMI-based emissions indicate that a much larger fraction of Algeria's methane emissions come from oil production than national reporting suggests. Additionally, we find that although in both regions diffuse area sources constitute the majority of emissions, relatively few space-detected super-emitters also provide a large contribution to the total area emissions (24 [12-40]% in Hassi R'Mel; 49 [27-71]% in Hassi Messaoud). The importance of both super-emitters and diffuse area sources indicates that mitigation efforts should address both the largest super-emitters, as well as include a wider portfolio of mitigation measures to improve oil and gas infrastructure in general. Our analysis shows that synergistic use of Sentinel-2 and TROPOMI, both with frequent global coverage, can produce a unique and detailed emission characterization of oil and gas production areas. Producing comparable emission characterizations for other areas is an important next step, as the contribution from super-emitters to total area emissions will differ between regions.

1 Introduction

Atmospheric methane has contributed at least a quarter to anthropogenic global warming since 1750 [Ocko et al., 2018]. The oil and gas (O/G) sector is responsible for around a quarter of anthropogenic methane emissions [Saunio et al., 2020]. Various studies [Zavala-Araiza et al., 2015, Cusworth et al., 2021a] have shown that O/G methane emissions have a heavy-tailed source distribution, with a small number of super-emitting point sources contributing a relatively large fraction of total emissions from O/G facilities. As addressing such super-emitters can be cost-beneficial, they are an attractive target for climate mitigation [Lauvaux et al., 2022]. In terms of regional emissions, diffuse area emissions also contribute significantly, and achieving optimal reductions in O/G methane emissions will require mitigation of these emissions as well [Lyon et al., 2015, Omara et al., 2022]. However, the relative contributions of diffuse area emissions and super-emitters to total O/G emissions remains uncertain, and will likely vary between regions. Here, we present a novel atmospheric emission inversion approach to estimate total area emissions along with the contributions from diffuse area emissions and super-emitters, which we apply to two important O/G production areas in Algeria.

Satellite instruments that measure atmospheric methane can provide valuable information in remote areas on O/G emissions, with regular revisit times that ground- or aircraft-based campaigns cannot match. This is especially important for O/G sources, since these are often intermittent [Cusworth et al., 2021a] and related to production activities in remote areas that are challenging to monitor. In recent years, the number of satellites that measure atmospheric methane has quickly expanded [Jacob et al., 2022]. In particular, the launch of the Tropospheric Monitoring Instrument (TROPOMI) on-board Sentinel-5P has been a major step forward, as it is the first instrument with daily, global coverage that can detect individual super-emissions above 8 t/hr [e.g., Schuit et al., 2023] due to its high precision and spatial resolution of up to 7.5 by 5.5 km^2 at nadir [Veefkind et al., 2012, Lorente et al., 2021]. However, in most cases it is not possible to link methane plumes detected by TROPOMI to individual facilities due to its spatial resolution.

Satellite instruments with a higher spatial resolution can serve a complementary role [Varon et al., 2019, Cusworth et al., 2021b]. For example, Sentinel-2 provides global coverage every 2-5 days at 20 m resolution and, as such, can help to trace large plumes to their sources [Drusch et al., 2012, Varon et al., 2021, Gorroño

et al., 2023]. However, due to its lower spectral resolution than TROPOMI (100-200 nm versus 0.25 nm), Sentinel-2 can only detect the largest point sources ($>1\text{-}2$ t/hr) over relatively uniform surfaces [Gorroño et al., 2023]. Targeting, hyperspectral instruments like the GHGSat constellation [Jervis et al., 2021], or hyperspectral instruments (e.g., PRISMA [Cusworth et al., 2019, Guanter et al., 2021]) provide additional information with better detection limits, but have limited coverage. Previous work has explored the synergy between these satellite instruments measuring at different spatial scales [e.g., Pandey et al., 2022], but has not yet integrated the different data streams to estimate total area emissions for longer time periods.

Estimating area emissions by combining these satellite data showing both super-emitters and diffuse area sources is not trivial. To estimate area sources at regional scale, inversions of atmospheric transport models are often used [e.g., Bergamaschi et al., 2009, Maasackers et al., 2019, Qu et al., 2021]. However, it is challenging to capture emission plumes in these relatively coarse region transport model simulations, due to limited model resolution, transport errors, and the large volume of satellite data that makes it time-intensive to verify transport model performance on individual emission events. On the other hand, studies that focus on emission events [e.g. Pandey et al., 2019, Cusworth et al., 2021b, Irakulis-Loitxate et al., 2022, Maasackers et al., 2022] or satellite-observed plumes in general [Lauvaux et al., 2022, Schuit et al., 2023] do not integrate these estimates in satellite-constrained area estimates. Therefore, the longterm area emission estimates do not fully exploit the increased data density of new satellites, while event-focused work only informs on emissions that result in large, concentrated plumes. An accurate assessment of total area emissions for longer time periods, combined with the characterization of relative contributions from diffuse area emissions and super-emitting point sources is essential for efficient emission mitigation of the overall emissions from the O/G sector.

In this study, we estimate the total area emissions, including the contribution from diffuse area emissions and super-emitting point sources ($>1\text{-}2$ t/hr; the Sentinel-2 detection limit) for two Algerian O/G production areas in 2020: Hassi R'Mel and Hassi Messaoud. In 2020, Algeria was the 10th-largest gas producer and the 16th-largest oil producer globally [EIA, 2023], and provided 10% of the gas imports of the European Union [McWilliams et al., 2021]. Accurate characterization and mitigation of the methane emissions associated with these imports fits the general strategy of the EU to reduce their greenhouse gas emissions. The two areas investigated in this work represent distinctly different production activities. Hassi R'Mel contains the largest gas field of Algeria (43% of national gas production in 2020 [Rystad Ucube, 2022]), oil production facilities (16% of national production), and acts as a processing hub for other Algerian O/G fields. Hassi Messaoud is mainly an oil production area (36% of national oil production), where frequent detections of methane emission events have been reported [Varon et al., 2019, Guanter et al., 2021, Sánchez-García et al., 2022]. In this study, we incorporate methane concentrations from TROPOMI and facility-level plumes detected by Sentinel-2 in a transport model inversion to provide a detailed characterization of the area emissions, separating the contribution from individual super-emitters ($>1\text{-}2$ t/hr) and the diffuse area source. In this way, we produce emissions estimates that provide information on the differences between an oil- and a gas-production dominated area, as well as on the relative roles of diffuse area emissions and super-emitters in both.

2 Materials and Methods

To estimate methane emissions in the two Algerian production fields, we first use Sentinel-2 methane plume detections to identify individual super-emitters. As such, we define super-emitters as sources detectable with Sentinel-2 ($>1\text{-}2$ t/hr). Based on Sentinel-2 methane enhancements, we use a mass-balance method to derive the emissions for individual plumes. We then perform a transport model (WRF-Chem) inversion based on TROPOMI data that includes the Sentinel-2 emission estimates as prior information on the super-emitting point sources. Additionally, our simulations include the O/G methane emissions from the bottom-up Scarpelli et al. [2022] emission inventory as a first estimate for diffuse emissions. The latter represent sources that are too small to be detected as individual sources in Sentinel-2, but which can be constrained as an aggregate in TROPOMI methane data, since TROPOMI has higher precision and integrates enhancements over a larger area. In the inversion, super-emitters and diffuse area emissions are optimized independently.

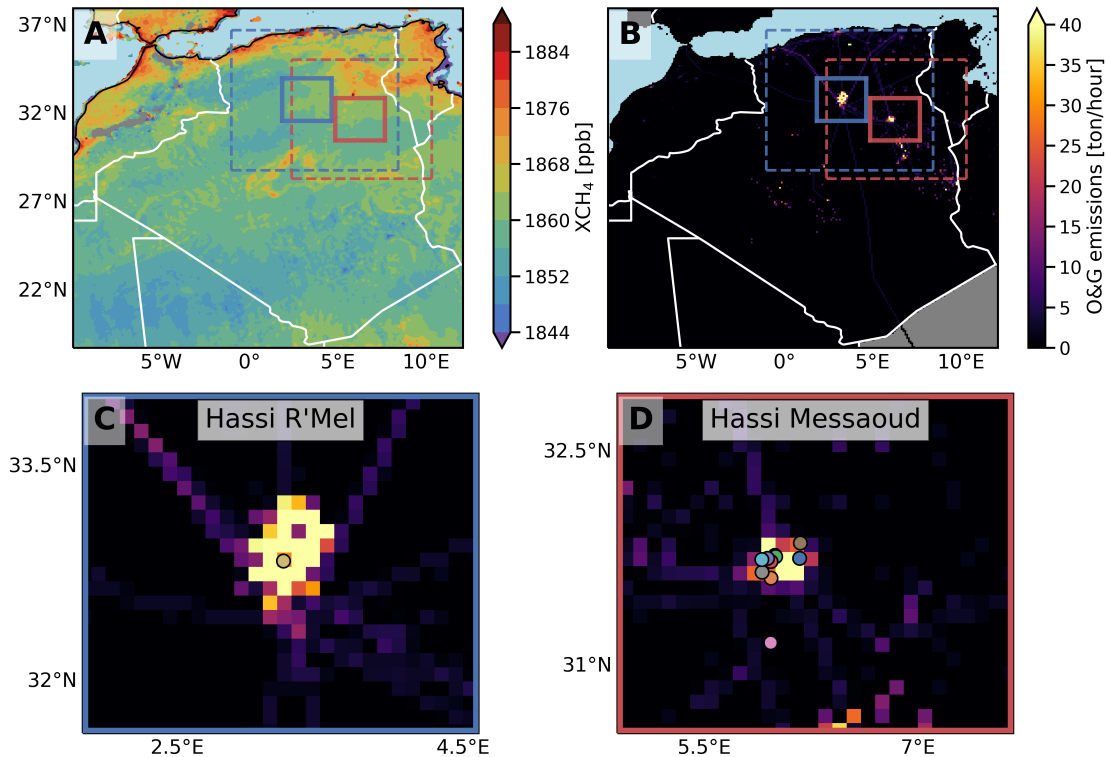


Figure 1: An overview of Algeria and our study domains. Panel A: average 2020 TROPOMI XCH₄ data over Algeria. Panel B: Bottom-up O/G methane emissions in Algeria [Scarpelli et al., 2022]. Panels A and B show inner (solid) and outer (dashed) zoom domains used in the WRF-Chem simulations for Hassi R'Mel (blue) and Hassi Messaoud (red). Panel C-D: Zoom-in of bottom-up emissions [Scarpelli et al., 2022] in the two inner zoom domains: Hassi R'Mel (C) and Hassi Messaoud (D). Sentinel-2 detected methane point source locations are marked with colored circles.

2.1 TROPOMI and Sentinel-2 satellite data

TROPOMI is an atmospheric monitoring instrument that provides daily global coverage of column-averaged, dry air mixing ratios of methane (XCH₄) at a resolution of 7.5 by 5.5 km² in nadir, based on measurements in the shortwave infrared (SWIR) spectrum at 2.3 μm [Veefkind et al., 2012, Lorente et al., 2021]. TROPOMI can detect large (> 8 t/hr) concentrated methane sources in a single overpass [Lauvaux et al., 2022, Schuit et al., 2023], and it frequently detects plumes in both of our study areas. We use version 2.04 of the TROPOMI-CH₄ product [Lorente et al., 2022]. We correct for along-track stripes following the FMD approach of Borsdorff et al. [2018], and apply a custom data quality filter (qa > 0.1; precision < 10 ppb; cloud fraction < 0.1; SWIR aerosol optical thickness < 0.1; see Fig 1 panel a). Using these filters, we find 224 and 238 days in 2020 with sufficient coverage for emission estimation (> 20 pixels per day) over Hassi R'Mel and Hassi Messaoud, respectively. The 2020-averaged TROPOMI methane field is shown in Fig. 1a. We note that some of the large-scale methane gradients are "artefacts" driven mostly by albedo gradients (e.g. in the north-east extending to the middle of Tunisia) and/or low coverage (near the coast). However, such effects in the two regions investigated here are small.

The Sentinel-2 mission is a constellation of two satellites, with the Multi Spectral Imager as their main instrument, which is a land and ocean surface imager with lower spectral (100-200 nm) but higher spatial resolution (20 m) than TROPOMI [Drusch et al., 2012]. Sentinel-2 provides global coverage with a revisit time of 2 to 5 days. Sentinel-2 has previously been used to study large methane point sources [Varon

et al., 2021, Irakulis-Loitxate et al., 2022, Ehret et al., 2022, Pandey et al., 2022]. Here, we retrieve XCH_4 enhancements using the multi-band-multi-pass (MBMP) method as described in Varon et al. [2021], where enhancements are calculated using the ratios between two SWIR spectral bands (one with stronger methane absorption than the other) on the day of interest normalized with a reference day. For each scene, we take the median over the MBMP with the ten best reference days, rather than use a single reference day. As shown by Gorroño et al. [2023], use of multiple reference days can make resultant plume detections less prone to surface reflectance variations than using a single day. We select the ten reference days as those with the most similar surface reflectance as the day of interest, based on the correlation with the day of interest in the red spectral band. Due to the use of only two spectral bands, Sentinel-2 can only detect methane enhancements (as opposed to absolute methane column concentrations) under favorable observation conditions as it is sensitive to surface albedo (e.g., buildings) and aerosol (e.g., smoke) features [Gorroño et al., 2023]. For high-albedo and relatively uniform surfaces, as those investigated in this study, the Sentinel-2 methane plume detection limit has been estimated at 1 to 2 t/hr depending on the wind conditions [Gorroño et al., 2023]. To better understand the (limitations of the) Sentinel-2 data, we also use five observations from the methane-designated GHGSat-C1 satellite instrument over Hassi Messaoud. GHGSat observes methane at 25-m resolution over $\sim 10 \times 15 \text{ km}^2$ spatial domains with a reported detection limit of $\sim 100 \text{ kg hr}^{-1}$ [ESA, 2022]. More details are provided in Supplement S3.

While Hassi R'Mel and most prominently Hassi Messaoud are areas with the strongest and most frequent plume signals in TROPOMI and Sentinel-2, Algeria does have additional areas with O/G production (Fig. 1B), where we observe methane plumes with TROPOMI and Sentinel-2. The largest of these are the fields south of the inner Hassi Messaoud domain (red solid square in Fig. 1A/B). However, near this field we find frequent interference from aerosols that affects the TROPOMI methane product and would make an inversion more complicated than in the other two regions. Therefore, we focus on the aforementioned two areas in our current analysis.

2.2 Sentinel-2 plume detection and emission estimates

We use Sentinel-2 to detect emissions from individual point sources and provide a first quantification of their emission rates using a mass-balance approach. For the detection of Sentinel-2 sources both the Hassi R'Mel and Hassi Messaoud areas were explored, partly guided by plume detections in TROPOMI data as in Schuit et al. [2023]. Once a super-emitter source is detected with Sentinel-2, we construct a 2020 timeseries for that source by manually labeling all scenes as either 'with plume', 'no plume', or 'bad data' (e.g., cloudy days). For all scenes with a plume, we calculate an emission source rate using the Integrated Mass Enhancement (IME) approach [Frankenberg et al., 2016, Varon et al., 2018]. We follow the approach described by Varon et al. [2019], including their effective wind speed calibration with ERA-5 10-m wind speeds [Hersbach et al., 2020], but we apply a different plume masking.

For our plume masking we only consider pixels in a 1075 m (1000 m downwind and 75 m upwind of the source) \times 500 m box downwind of the source. Since we find that the wind direction in the ERA-5 10-m wind data often does not align with the plume direction, we determine the plume direction based on the observed Sentinel-2 methane plume. To do so, we take the pixel with highest methane enhancement within a 10-pixel ($\sim 200 \text{ m}$) square around the source and then we iteratively include adjacent pixels with methane enhancements higher than 1.8 standard deviations above the scene average. We then calculate the plume direction as an average of the angle between the source and these selected pixels, weighted by the pixel distance from the source. Finally, we select all pixels in the resulting box that are 1.8 SD above the scene average as part of our own plume mask. The background enhancement is calculated as the average over a 500 m by 500 m box placed 150 m upwind of the plume. Fig. S1 shows the resulting boxes and plume masks for one plume detection per source location. We assume a fixed 50% error on the Sentinel-2 emission estimates. This uncertainty can vary per plume detection, with uncertainty increasing at lower wind speeds, and 50% is somewhat conservative [Varon et al., 2021]. Therefore, we vary this error between 30% and 70% in the sensitivity ensemble (see Section 2.4).

2.3 WRF-Chem transport model

We use the Weather Research and Forecast model coupled to Chemistry (WRF-Chem) version 4.1 [Powers et al., 2017] to simulate the atmospheric transport of methane emissions in the Hassi R'Mel and Hassi Messaoud areas separately. For both areas, we include three nested domains centered on the respective O/G field, with each domain consisting of 100 by 100 grid cells with a resolution of 3, 9 and 27 km, respectively (Fig. 1). We use methane fields from the Copernicus Atmospheric Monitoring Service (CAMS) at 0.25° by 0.25° resolution for initialization and as 6-hourly boundary conditions [Koffi and Bergamaschi, 2018]. Meteorology in the WRF-Chem simulations is driven at the boundaries by meteorological fields provided by the National Centers for Environmental Prediction (NCEP) [National Centers for Environmental Prediction, National Weather Service, NOAA, U.S. Department of Commerce, 2000]. We sample the 3-D CH_4 simulation output at the TROPOMI pixel locations and the vertical levels of the TROPOMI averaging kernel, after which we apply the averaging kernels to retrieve simulated XCH_4 values that can be compared to TROPOMI data in the inversion.

For the quality of our inversion estimate it is important to obtain a good match between simulated and observed plumes. Therefore, following Maasackers et al. [2022], we perform simulations for each domain with five different planetary boundary layer (PBL) schemes (Table S1; Fig 2). For all other settings we use the CONUS physics suite. Additionally, we sample the simulations at 11, 12 and 13 UTC, which roughly covers the variation in the TROPOMI overpass times over the areas. This approach produces an ensemble of simulated scenes (15 per day) from which we select the optimal plume match on each day for the inversion (Sect. 2.4 and Fig. 2).

Prior emissions for the WRF simulations are based on Sentinel-2 for super-emitting point sources ($> 1 - 2$ t/hr; the Sentinel-2 detection limit) and on Scarpelli et al. [2022] for diffuse area emissions, even though the latter is supposed to encapsulate total emissions. Scarpelli et al. [2022] provides a global oil, gas and coal methane emission inventory for 2019 at $0.1 \times 0.1^\circ$ resolution. National total methane emissions are consistent with those reported to United Nations Framework Convention on Climate Change (UNFCCC), extrapolating to 2019 when only historic reports are available, and are spatially distributed using a variety of infrastructure datasets. For Algeria, 95% of O/G methane emissions are reported to come from gas exploitation and distribution, and only 5% from oil activity [Algeria, 2010].

2.4 Inversion framework

We obtain our optimized emission estimate from an inversion where prior emissions (individual super-emitters and the diffuse area source) and the CAMS background are scaled to best reproduce TROPOMI data. For this, we solve the analytical Bayesian problem [Jacob et al., 2016] of minimizing a cost function J to retrieve an optimal state vector $\hat{\mathbf{x}}$ as:

$$\hat{\mathbf{x}} = \mathbf{x}_A + \mathbf{S}_A \mathbf{K}^T (\mathbf{K} \mathbf{S}_A \mathbf{K}^T + \mathbf{S}_O^{-1})^{-1} (\mathbf{y} - \mathbf{K} \mathbf{x}_A), \quad (1)$$

with $\hat{\mathbf{x}}$ the optimized state vector, \mathbf{x}_A the prior state vector, \mathbf{S}_A the prior error covariance matrix, \mathbf{K} the Jacobian, \mathbf{y} the observational vector and \mathbf{S}_O the observational error covariance matrix. The state vector \mathbf{x} includes per-orbit scaling factors for the CAMS background, daily emissions for each point source, and monthly diffuse emissions. We subdivide the diffuse emissions in the inner domain in a 6 by 6 grid (36 elements; ~ 50 by 50 km^2 each) and in the middle and outer domain in a 4 by 4 grid, optimizing each grid element independently. We optimize the CAMS background per orbit, because on some days the domain is covered by two TROPOMI overpasses, and the gradients between these overpasses are not always captured in the CAMS boundary conditions. We assume a 50% error on the Sentinel-2 based emission estimates (see Sect 2.2), as well as on the prior diffuse emissions. Here and in previous work [Maasackers et al., 2022] we find that the CAMS background needs to be adjusted upwards by 3-5% relative to the prior, and we therefore assume a 10% error on the CAMS background. We assume a fixed observational error of 15 ppb on individual TROPOMI XCH_4 columns, which is based on the standard deviation of the difference between the prior model and the observations. We aggregate TROPOMI data to a $0.2^\circ \times 0.2^\circ$ grid for the model-observation

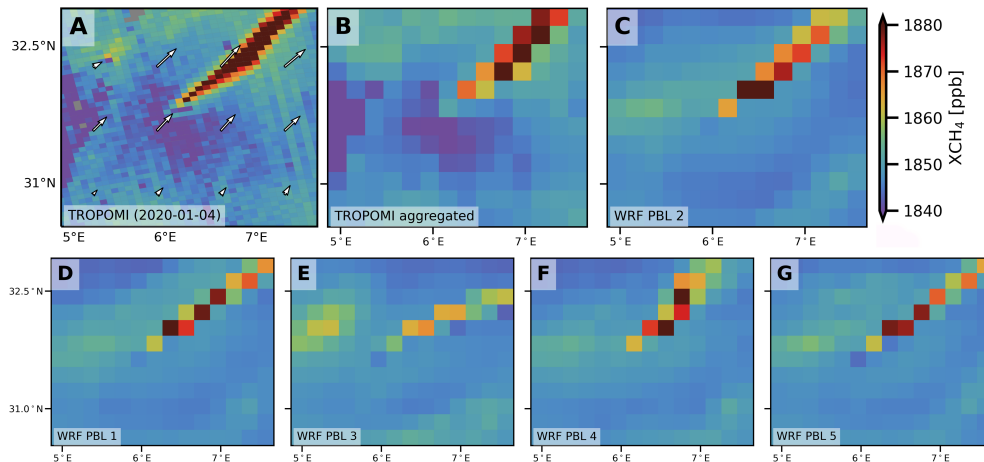


Figure 2: A large methane plume as observed by TROPOMI on 4 Jan 2020 (panel a), regridded to 0.2° resolution (panel b). Panels c-g show the corresponding five WRF-Chem simulations with different PBL schemes (sampled at 12 UTC). To select the best-performing PBL scheme, we select the scheme with the lowest posterior cost for that day: in this case PBL scheme 2 (panel c; the Mellor-Yamada-Janjic TKE scheme).

comparison, to reduce the impact of small differences between simulated and observed plumes (Fig. 2 a and b). We assume that prior errors (\mathbf{S}_A) and observational errors (\mathbf{S}_O) are uncorrelated.

To ensure the best match between simulated and observed plumes, we perform WRF simulations with 5 PBL schemes (Section 2.3). To find the best PBL scheme per day, we perform two sets of preliminary inversions. Firstly, we perform an inversion for 2020 based on one PBL scheme to get optimised monthly diffuse emissions. These are then used in daily inversions for each PBL scheme and each sample timestep (for a total of 15 inversions per day), to select the PBL scheme producing the best match with TROPOMI for each day, based on the lowest posterior cost (Fig. 2). Additionally, in selecting the optimal PBL scheme preference was given to the daily inversions with positive posterior point source emissions. We then perform the final inversion in which we optimize the full state vector, with the Jacobian \mathbf{K} constructed using one optimal PBL scheme and sampling time for each day. We remove days in which the final inversion produces negative point source emissions from the analysis (caused by a poor fit to the observations), which has only a small effect (<5%) on the annual average source rates.

To estimate uncertainties, we report the range of a sensitivity ensemble of different inversion configurations (Table 1). We find that the optimized emissions are especially sensitive to scaling the priors. Therefore, we independently vary the point-source and diffuse priors in our ensemble with $\pm 50\%$ and also vary the prior error between 30% and 70%. Additionally, in some months (e.g., May 2020 in Hassi R'Mel) monthly emissions are disproportionately influenced by observations from a single day, and removing this day from the inversion results in significantly different monthly emissions. We therefore include a sensitivity inversion in which we exclude the day with the largest contribution to the cost function J . Finally, we add a sensitivity inversion where we use the second-best performing PBL for each day.

To assess the performance of the inverse system and the representativeness of the sensitivity ensemble we performed an Observation System Simulation Experiment (OSSE), where we used one PBL simulation as truth, and estimate emissions based on the other four. The OSSE is especially useful to assess the influence of transport errors on the final emission estimate. For example, a mismatch between simulated and observed plumes can lead to a large error in estimated emissions, but does not necessarily result in a large spread in the sensitivity ensemble. In the OSSE, we find that daily estimated (point source) emissions have large errors (50%), but these errors mostly average out on monthly and annual scales to 25% and 15%, respectively. Point sources are generally underestimated (on average by 20%), while the bias for diffuse emissions is much

smaller. This is because point source plumes are very concentrated and therefore difficult to capture in the simulation, while diffuse plumes are more likely to have at least some overlap with observed plumes. This result implies that in our approach we give a conservative estimate of the contribution from super-emitters. At the same time, the uncertainty in estimated total and diffuse area emissions is limited by TROPOMI’s precision as well as the inversion model. A full description of the OSSE analysis is given in Supp. 1.

Parameter	Reference	Low	High
Scale point sources	1.0	0.5	1.5
Scale diffuse sources	1.0	0.5	1.5
Prior error emissions	50%	30%	70%
Aggregation resolution	0.2 °	0.1 °	0.3 °
Other ensemble members			
Exclude for each month the day with the most observational weight.			
Use the second-best PBL scheme for each day in the optimization.			

Table 1: Ensemble of inversions that is used to quantify posterior uncertainties.

3 Results & Discussion

3.1 Sentinel-2 detections and emission estimates

In our Sentinel-2 analysis, we detect one super-emitter source in the Hassi R'Mel field and ten in the Hassi Messaoud field (Fig. 3 and Fig. S1), with a combined total of 347 plume detections in 2020. Since two Hassi Messaoud sources are close together (<1km), we group them as one cluster (M03) in our analysis. The IME-based emission estimates (Fig. 3) show that during 2020 some sources emit on nearly every day with Sentinel-2 coverage (e.g., at M03a we detect plumes on 90% of days with coverage; see also Table S3), while others emit above the Sentinel-2 detection limit only on a few days (e.g., one day at M07). By far the largest emissions from a single source are detected at M06 on Jan 4 (29.8 ± 14.9 t/hr) and Jan 7 (68.4 ± 34.2 t/hr), while the Jan 9 Sentinel-2 overpass reveals flaring at this location (also reported in Pandey et al. [2022]). TROPOMI shows large plumes from Jan 3 to Jan 8. This event demonstrates the complementarity of the Sentinel-2 high-spatial resolution with the daily TROPOMI coverage. Source M08 has been described in Varon et al. [2021] as emitting methane consistently over a ten-month period, ending in August 2020, which is confirmed in our analysis, and we produce emission estimates consistent with theirs (Fig. S1).

Sentinel-2 can only be used to detect the largest super-emitters (>1-2 t/hr [Gorriño et al., 2023]). Inspection of targeted GHGSat data, which has a better detection limit than Sentinel-2, reveals an additional source location near M06 (see Supp. 3). The emission rates calculated from the GHGSat data are below or close to the Sentinel-2 detection limit (0.4-1.2 t/hr). Sentinel-2 does show plume signals at this location on 6 days in 2020 (no overlap with GHGSat detections), but since this source was identified after performing the WRF simulations, it is not included in the rest of our analysis. This result shows both the potential importance of large point sources emitting below the Sentinel-2 detection limit, included in this work in the diffuse area source, as well as the challenge in comprehensively identifying all emission signals in Sentinel-2 over a large area.

Based on visual imagery (mostly from ESRI World Imagery [ESRI et al., 2022]), we identify ten locations as flares, and one as a production well (M06; see also [Pandey et al., 2022]) (full list in Table S3). Since most sources are found in the oil-production dominated Hassi Messaoud area, our results indicate that most emissions from detected super-emitting point sources come from unlit flares related to oil activity.

3.2 Hassi Messaoud and Hassi R'Mel emission estimates

Our inversion finds a large correction to the CAMS boundary conditions (3.4% on average), but also significantly improves the agreement between model and TROPOMI through corrections to the emissions, both in terms of mean absolute bias (59.13 ppb to 0.05 ppb) and correlation ($r^2 = 0.85$ when only the optimized variations in CAMS are included; to $r^2 = 0.89$ when emission optimized emission variations are also included). Fig. 4 and Table S2 show the emission estimates for Hassi R'Mel and Hassi Messaoud, where we distinguish between super-emitting point sources and diffuse area sources. The two regions show different adjustments from the inversion: in Hassi R'Mel (gas-production dominated), prior emissions are significantly too high with and without point sources, while in Hassi Messaoud (oil-production dominated) they are approximately correct. The prior (mainly diffuse) emissions in Hassi R'Mel are high (0.39 Tg/yr), which would produce large methane signals in TROPOMI. Since we find only a single point source (5.3 t/hr; see Table S3) in Sentinel-2 and small methane enhancements in TROPOMI, we consider the strong downward adjustment to 0.16 [0.11-0.22] Tg/yr highly plausible. Our diffuse posterior emission estimate for Hassi Messaoud (0.11 [0.06-0.15] Tg/yr) aligns well with the bottom-up prior emissions from Scarpelli et al. [2022]. However, the Scarpelli et al. [2022] inventory is supposed to represent all O/G emissions, and if we include super-emitters (0.11 [0.06-0.17] Tg/yr), we find 79 [4-188]% higher emissions.

If we combine the methane emission estimates with marketable gas production data for each field (as in e.g., Alvarez et al. [2018]), we find methane intensities of 0.9 [0.7-1.1] % and 116.6 [70.0-148.8] % for Hassi R'Mel and Hassi Messaoud, respectively (assuming 80% methane content for natural gas). We note that these methane intensities are based on marketable production [Rystad Ucube, 2022]: gross gas production might be higher, which would result in lower intensities. Following Schneising et al. [2020], we additionally

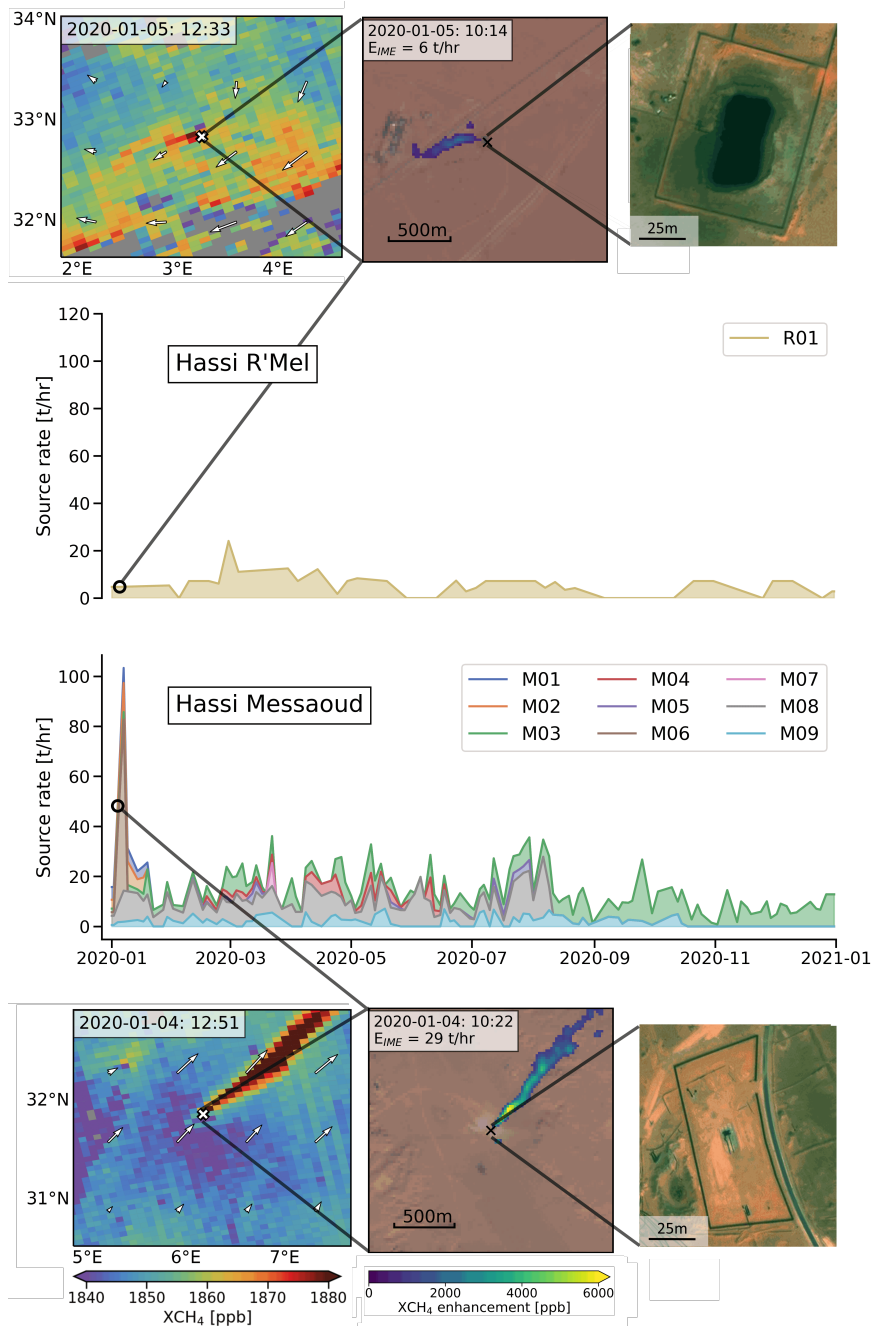


Figure 3: Daily source rate estimates based on an IME analysis of the Sentinel-2 methane data. The top and bottom panels show methane plumes as observed by TROPOMI (left; wind vectors showing 10-m ERA-5 winds [Hersbach et al., 2020]), Sentinel-2 (middle) and Bing imagery (right; ©Vexcel Imaging, 2023), for one day in Hassi R'Mel (top) and Hassi Messaoud (bottom) that have both Sentinel-2 and TROPOMI coverage. For the emission timeseries, we linearly interpolate between days with Sentinel-2 coverage. Emission timeseries are shown as the sum of all sources in each respective domain, where colors differentiate between the contributions of the different clusters of super-emitting point sources (also shown in Fig. 1).

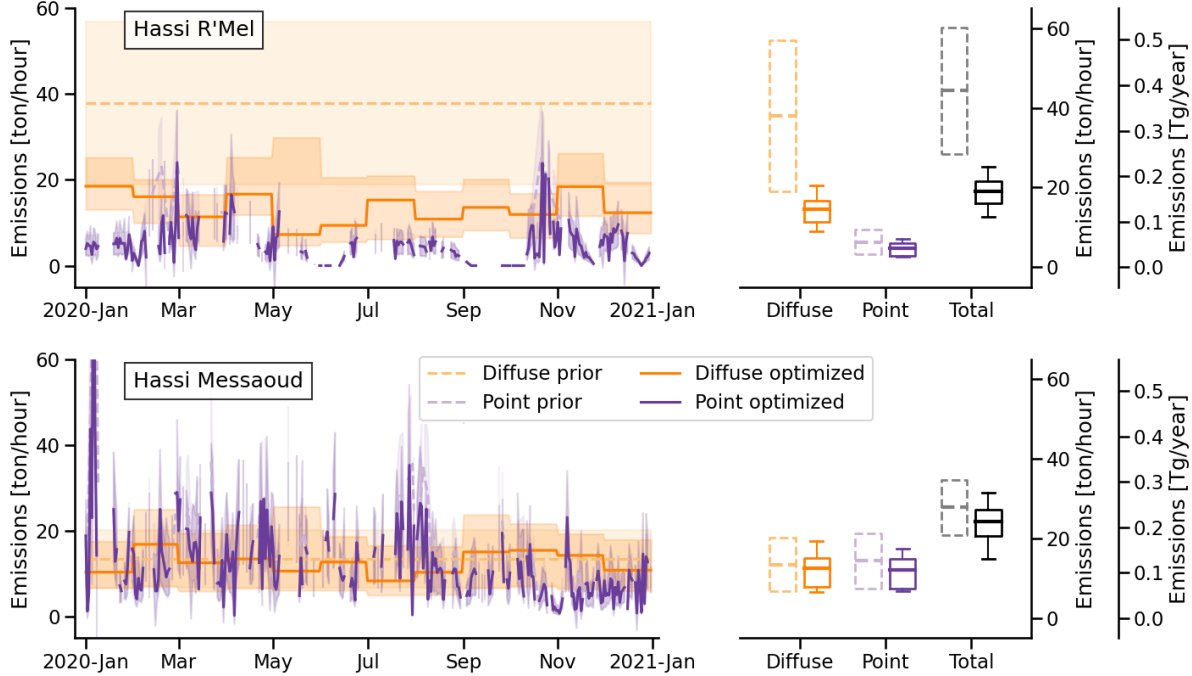


Figure 4: Prior (dashed lines) and posterior (solid lines) methane emission estimates for point (purple) and diffuse (orange) sources, in Hassi R'Mel and Hassi Messaoud. Left panels show the emission timeseries over 2020, with daily emissions from point sources and monthly emissions from diffuse area sources. The right panels show the annual mean estimates for each category, as well as their combined total. Uncertainty margins indicate the full range of the sensitivity ensemble, while the solid lines indicate the result from the reference inversions.

calculate a methane intensity based on the combined oil and gas production in each area. For this, we convert gas production and methane emissions to barrels of oil equivalent (boe) using a conversion factor of 6000 cubic feet per boe [EIA, 2019]. Using this approach, we calculate methane intensities of 0.5 [0.4-0.7] % and 1.1 [0.7-1.4] % in Hassi R'Mel and Hassi Messaoud respectively. Including oil production in the methane intensity is especially relevant in Hassi Messaoud, where production is oil-dominated.

When we assume that O/G methane emissions in Algeria scale linearly with production, and we combine national total O/G production with the O/G production in Hassi Messaoud and Hassi R'Mel [Rystad Ucube, 2022], we find national 2020 emissions of 0.53 [0.39-0.66] Tg/yr (oil) and 0.17 [0.09-0.28] Tg/yr (gas) for a total of 0.70 [0.47-94] Tg/yr, where we distinguish between oil and gas based on the O/G production ratio in the two domains. To test the sensitivity of the upscaling procedure, we alternatively use the ratio between the sum of prior O/G emissions in the two regions and national total O/G emissions [Scarpelli et al., 2022]. Using this ratio, we estimate Algerian emissions at 0.89 [0.56-1.18] Tg/yr. For the upscaling we only included the upstream (exploration, production, and processing) and midstream (transmission and storage) sectors of prior emissions: Scarpelli et al. [2022] estimate downstream emissions at 0.18 Tg/yr, which should be added to our estimates to get total oil/gas emissions. Both our estimates are consistent with Algeria's last UNFCCC-reported O/G methane emissions of 1.0 Tg/yr for 2000 [Algeria, 2010]. However, our results suggest that substantially more methane emissions come from oil production ($\sim 75\%$ of total emissions) than suggested in this report (5%). We note that national reporting updated for more recent years would make this comparison more insightful. If we upscale using prior emissions based on only Hassi R'Mel or Hassi Messaoud the best estimate changes from 0.89 Tg/yr to 0.61 or 1.60 Tg/yr, respectively, which indicates the significant uncertainty of estimating Algerian emissions based on a subset of fields.

Previous satellite-based transport model inversions have estimated Algerian methane emissions at 1.82

[1.68-1.96] Tg/yr for 2017 [Western et al., 2021] and at 3.7 ± 0.3 Tg/yr for 2019 [Worden et al., 2022], based on GOSAT, and at 3.5 [2.4-4.4] Tg/yr for 2019, based on TROPOMI [Chen et al., 2023]. Attribution of these national total emissions to different source sectors differs significantly: Western et al. [2021] attribute 80% of total Algerian emissions to O/G activity in the prior, but do not revise this percentage based on the inversion; Worden et al. [2022] estimate O/G emissions at 3.2 Tg/yr; Chen et al. [2023] estimate lower O/G emissions at 2.09 Tg/yr, and separately estimate O/G upstream and midstream emissions at 1.60 and 0.29 Tg/year, respectively. In general, these emission estimates are somewhat higher than what we report here, but, as indicated above, our national upscaling based on only two fields introduces additional uncertainty. Moreover, Algerian oil and gas production in 2020 were lower than in previous years (e.g., by 4% (gas) and 8% (oil) compared to 2019 [Rystad Ucube, 2022]). We also use the latest TROPOMI version (2.04), which has improved accounting for albedo gradients such as those seen near Hassi R'Mel [Lorente et al., 2022], which can introduce differences between studies. While we do consider our emission estimate conservative (e.g., based on the OSSE; see Supp. 1), we find an overall good posterior match between the annual-averaged simulated methane concentration fields and TROPOMI (annual mean bias of 0.05 ppb), which provides confidence in our emission estimate. To better compare our emission estimate to more conventional area inversions that only optimize diffuse emissions at a coarser resolution, we additionally performed an inversion in which we coarsen TROPOMI to $1.0^\circ \times 1.0^\circ$ resolution, include only annual diffuse emissions and optimize the background monthly. When we do this, we find comparable posterior emissions to our reference inversion ($\sim 10\%$ difference; see Table S3) which confirms the robustness of our emission estimates.

Part of the novelty in our approach comes from the distinction between point and diffuse area sources. We find that in Hassi Messaoud large point sources ($> 1\text{-}2$ t/hr individually) contribute more to the total emissions (49 [27-71]%) than in Hassi R'Mel (24 [12-40]%) and diffuse area emissions contribute significantly to the total regional emissions in both regions. Some of the Sentinel-2-detected sources emit frequently, and addressing these sources is a logical target for emission mitigation. The posterior differentiation between point and diffuse sources is in large part informed by the Sentinel-2 analysis, since distinguishing between them in the TROPOMI-based inversion is difficult. For example, the prior uncertainty in the point source contribution is only reduced by $\sim 20\%$. This is in part because we coarsen the TROPOMI data to $0.2^\circ \times 0.2^\circ$ resolution, which reduces the difference between point and diffuse signals in the TROPOMI data. In addition, the differences between point source and diffuse signals are often smaller than the model transport errors. This might be different in other areas where production is more spread out.

The advantage of our approach, however, is that we integrate the information from Sentinel-2 and TROPOMI in one consistent statistical framework, where Sentinel-2 provides information on the importance of point sources and TROPOMI on the total area emissions. This is an improvement on previous work, where either only (gridded) area emissions are estimated [Varon et al., 2022, Chen et al., 2022], or point source emission estimates are compared to national inventories to estimate their relative contribution [Lauvaux et al., 2022].

The resulting emission estimates from our methodology provide valuable and unique information on total area emissions as well as the contributions of diffuse area emissions and super-emitters, and their temporal variability. The developed system can be applied to other emission regions, realizing that each area will have its own challenges with respect to the satellite data that need to be considered, and our approach can be aided by automated plume detection [Lauvaux et al., 2022, Schuit et al., 2023]. The availability of global data from both TROPOMI and Sentinel-2 makes such an approach feasible for many areas. For Algeria we find that emissions in Hassi R'Mel, the largest Algerian gas field, are overestimated in Scarpelli et al. [2022] by 53 [24-73]%, and emissions in Hassi Messaoud (oil-dominated) are underestimated by 79 [4-188]%. Our Sentinel-2 analysis shows that most super-emitters in the two Algerian fields are unlit flares (10 out of 11). The difference between the relative contribution from super-emitting and diffuse sources for the two fields highlights the importance of assessing this distribution for individual areas around the world. Additionally, designated methane satellites such as GHGSat (see Supp. 3) and ground-based campaigns can help understand the distribution of emissions below the Sentinel-2 detection limit (1-2 t/hr), while satellites with an intermediate resolution (100-500 m), such as Sentinel-3 and the upcoming MethaneSAT mission, can bridge the gap between TROPOMI and individual source detections [e.g., Pandey et al., 2022]. Such information on the

emission distribution per O/G production area is highly relevant for effective emission mitigation. For Algeria, we find that addressing the largest super-emitters can significantly reduce O/G emissions. However, the majority of emissions in both areas comes from sources that are individually below the Sentinel-2 detection limit (1-2 t/hr), which means that to optimally reduce region-wide emissions, mitigation of diffuse area emissions will also be needed and will likely require general infrastructure improvements beyond addressing the largest super-emitters.

Acknowledgements

The authors thank the team that realized the TROPOMI instrument and its data products, consisting of the partnership between Airbus Defense and Space Netherlands, KNMI, SRON, and TNO, commissioned by NSO and ESA. Sentinel-5 Precursor is part of the EU Copernicus program, Copernicus (modified) Sentinel-2 and Sentinel-5P data (2020) have been used. We thank SURF (www.surf.nl) for the support in using the National Supercomputer Snellius. SN and BN acknowledge funding through the UNEP CCAC Methane Studies and the Environmental Defense Fund (EDF). AL and TB acknowledge funding through the TROPOMI national program through NSO.

Author contributions

SN and JDM developed the conceptual ideas for the study. SN performed the TROPOMI/WRF analysis with input from BN and JDM. RG and MO provided the production analysis and supported the contextualization of the project. RS and AV performed the Sentinel-2 analysis with input from SP, II, and LG. AL and TB provided the TROPOMI data and associated support. SN wrote the manuscript with inputs from all co-authors.

References

- Algeria. Inventaire national des émissions de gaz à effet de serre de l'année 2000. https://unfccc.int/sites/default/files/resource/Algeria_GHG%20Inventory.pdf, 2010.
- R. A. Alvarez, D. Zavala-Araiza, D. R. Lyon, D. T. Allen, Z. R. Barkley, A. R. Brandt, K. J. Davis, S. C. Herndon, D. J. Jacob, A. Karion, E. A. Kort, B. K. Lamb, T. Lauvaux, J. D. Maasakkers, A. J. Marchese, M. Omara, S. W. Pacala, J. Peischl, A. L. Robinson, P. B. Shepson, C. Sweeney, A. Townsend-Small, S. C. Wofsy, and S. P. Hamburg. Assessment of methane emissions from the U.S. oil and gas supply chain. *Science*, 361(6398):186–188, 2018. doi: 10.1126/science.aar7204. URL <https://www.science.org/doi/abs/10.1126/science.aar7204>.
- P. Bergamaschi, C. Frankenberg, J. F. Meirink, M. Krol, M. G. Villani, S. Houweling, F. Dentener, E. J. Dlugokencky, J. B. Miller, L. V. Gatti, A. Engel, and I. Levin. Inverse modeling of global and regional CH₄ emissions using SCIAMACHY satellite retrievals. *Journal of Geophysical Research: Atmospheres*, 114(D22), 2009. doi: <https://doi.org/10.1029/2009JD012287>.
- T. Borsdorff, J. Aan de Brugh, H. Hu, I. Aben, O. Hasekamp, and J. Landgraf. Measuring Carbon Monoxide With TROPOMI: First Results and a Comparison With ECMWF-IFS Analysis Data. *Geophysical Research Letters*, 45(6):2826–2832, 2018. doi: <https://doi.org/10.1002/2018GL077045>.
- Z. Chen, D. J. Jacob, H. Nesser, M. P. Sulprizio, A. Lorente, D. J. Varon, X. Lu, L. Shen, Z. Qu, E. Penn, and X. Yu. Methane emissions from China: a high-resolution inversion of TROPOMI satellite observations. *Atmospheric Chemistry and Physics*, 22(16):10809–10826, 2022. doi: 10.5194/acp-22-10809-2022. URL <https://acp.copernicus.org/articles/22/10809/2022/>.

- Z. Chen, D. J. Jacob, R. Gautam, M. Omara, R. N. Stavins, R. C. Stowe, H. O. Nesser, M. P. Sulprizio, A. Lorente, D. J. Varon, X. Lu, L. Shen, Z. Qu, D. C. Pendergrass, and S. Hancock. Satellite quantification of methane emissions and oil/gas methane intensities from individual countries in the Middle East and North Africa: implications for climate action. *EGUsphere*, 2023:1–42, 2023. doi: 10.5194/egusphere-2022-1504. URL <https://egusphere.copernicus.org/preprints/egusphere-2022-1504/>.
- D. H. Cusworth, D. J. Jacob, D. J. Varon, C. Chan Miller, X. Liu, K. Chance, A. K. Thorpe, R. M. Duren, C. E. Miller, D. R. Thompson, C. Frankenberg, L. Guanter, and C. A. Randles. Potential of next-generation imaging spectrometers to detect and quantify methane point sources from space. *Atmospheric Measurement Techniques*, 12(10):5655–5668, 2019. doi: 10.5194/amt-12-5655-2019. URL <https://amt.copernicus.org/articles/12/5655/2019/>.
- D. H. Cusworth, R. M. Duren, A. K. Thorpe, W. Olson-Duvall, J. Heckler, J. W. Chapman, M. L. Eastwood, M. C. Helmlinger, R. O. Green, G. P. Asner, P. E. Dennison, and C. E. Miller. Intermittency of Large Methane Emitters in the Permian Basin. *Environmental Science & Technology Letters*, 8(7):567–573, 2021a. doi: 10.1021/acs.estlett.1c00173.
- D. H. Cusworth, R. M. Duren, A. K. Thorpe, S. Pandey, J. D. Maasackers, I. Aben, D. Jervis, D. J. Varon, D. J. Jacob, C. A. Randles, R. Gautam, M. Omara, G. W. Schade, P. E. Dennison, C. Frankenberg, D. Gordon, E. Lopinto, and C. E. Miller. Multisatellite Imaging of a Gas Well Blowout Enables Quantification of Total Methane Emissions. *Geophysical Research Letters*, 48(2):e2020GL090864, 2021b. doi: <https://doi.org/10.1029/2020GL090864>. URL <https://agupubs.onlinelibrary.wiley.com/doi/abs/10.1029/2020GL090864>. e2020GL090864 2020GL090864.
- M. Drusch, U. Del Bello, S. Carlier, O. Colin, V. Fernandez, F. Gascon, B. Hoersch, C. Isola, P. Laberinti, P. Martimort, A. Meygret, F. Spoto, O. Sy, F. Marchese, and P. Bargellini. Sentinel-2: ESA’s Optical High-Resolution Mission for GMES Operational Services. *Remote Sensing of Environment*, 120:25–36, 2012. ISSN 0034-4257. doi: <https://doi.org/10.1016/j.rse.2011.11.026>. URL <https://www.sciencedirect.com/science/article/pii/S0034425712000636>. The Sentinel Missions - New Opportunities for Science.
- T. Ehret, A. De Truchis, M. Mazzolini, J.-M. Morel, A. d’Aspremont, T. Lauvaux, R. Duren, D. Cusworth, and G. Facciolo. Global Tracking and Quantification of Oil and Gas Methane Emissions from Recurrent Sentinel-2 Imagery. *Environmental Science & Technology*, 56(14):10517–10529, 2022. doi: 10.1021/acs.est.1c08575. PMID: 35797726.
- EIA. U.s. energy information administration: The distribution of u.s. oil and natural gas wells by production rate. https://www.eia.gov/petroleum/wells/pdf/full_report.pdf, 2019.
- EIA. U.S. Energy Information Administration: International Energy Statistics, 2023. URL <https://www.eia.gov/international/data/world>. last access: January 2023.
- G. ESA. GHGSat mission overview, 2022. URL <https://earth.esa.int/eogateway/missions/ghgsat>.
- ESRI, Maxar, E. Geographics, and the GIS User Community. ESRI world imagery, 2022. URL https://services.arcgis.com/ArcGIS/rest/services/World_Imagery/MapServer.
- C. Frankenberg, A. K. Thorpe, D. R. Thompson, G. Hulley, E. A. Kort, N. Vance, J. Borchardt, T. Krings, K. Gerilowski, C. Sweeney, S. Conley, B. D. Bue, A. D. Aubrey, S. Hook, and R. O. Green. Airborne methane remote measurements reveal heavy-tail flux distribution in Four Corners region. *Proc. Natl. Acad. Sci. U. S. A.*, 113:9734, 2016.
- J. Gorroño, D. J. Varon, I. Irakulis-Loitxate, and L. Guanter. Understanding the potential of Sentinel-2 for monitoring methane point emissions. *Atmospheric Measurement Techniques*, 16(1):89–107, 2023. doi: 10.5194/amt-16-89-2023. URL <https://amt.copernicus.org/articles/16/89/2023/>.

- L. Guanter, I. Irakulis-Loitxate, J. G. no, E. Sánchez-García, D. H. Cusworth, D. J. Varon, S. Cogliati, and R. Colombo. Mapping methane point emissions with the PRISMA spaceborne imaging spectrometer. *Remote Sensing of Environment*, 265:112671, 2021. ISSN 0034-4257. doi: <https://doi.org/10.1016/j.rse.2021.112671>. URL <https://www.sciencedirect.com/science/article/pii/S0034425721003916>.
- H. Hersbach, B. Bell, P. Berrisford, S. Hirahara, A. Horányi, J. Muñoz-Sabater, J. Nicolas, C. Peubey, R. Radu, D. Schepers, A. Simmons, C. Soci, S. Abdalla, X. Abellan, G. Balsamo, P. Bechtold, G. Biavati, J. Bidlot, M. Bonavita, G. De Chiara, P. Dahlgren, D. Dee, M. Diamantakis, R. Dragani, J. Flemming, R. Forbes, M. Fuentes, A. Geer, L. Haimberger, S. Healy, R. J. Hogan, E. Hólm, M. Janisková, S. Keeley, P. Laloyaux, P. Lopez, C. Lupu, G. Radnoti, P. de Rosnay, I. Rozum, F. Vamborg, S. Villaume, and J.-N. Thépaut. The ERA5 global reanalysis. *Quarterly Journal of the Royal Meteorological Society*, 146(730):1999–2049, 2020. doi: <https://doi.org/10.1002/qj.3803>. URL <https://rmets.onlinelibrary.wiley.com/doi/abs/10.1002/qj.3803>.
- I. Irakulis-Loitxate, L. Guanter, J. D. Maasackers, D. Zavala-Araiza, and I. Aben. Satellites Detect Abatable Super-Emissions in One of the World’s Largest Methane Hotspot Regions. *Environmental Science & Technology*, 56(4):2143–2152, 2022. doi: 10.1021/acs.est.1c04873. PMID: 35102741.
- D. J. Jacob, A. J. Turner, J. D. Maasackers, J. Sheng, K. Sun, X. Liu, K. Chance, I. Aben, J. McKeever, and C. Frankenberg. Satellite observations of atmospheric methane and their value for quantifying methane emissions. *Atmospheric Chemistry and Physics*, 16(22):14371–14396, 2016. doi: 10.5194/acp-16-14371-2016. URL <https://acp.copernicus.org/articles/16/14371/2016/>.
- D. J. Jacob, D. J. Varon, D. H. Cusworth, P. E. Dennison, C. Frankenberg, R. Gautam, L. Guanter, J. Kelley, J. McKeever, L. E. Ott, B. Poulter, Z. Qu, A. K. Thorpe, J. R. Worden, and R. M. Duren. Quantifying methane emissions from the global scale down to point sources using satellite observations of atmospheric methane. *Atmospheric Chemistry and Physics*, 22(14):9617–9646, 2022. doi: 10.5194/acp-22-9617-2022. URL <https://acp.copernicus.org/articles/22/9617/2022/>.
- D. Jervis, J. McKeever, B. O. A. Durak, J. J. Sloan, D. Gains, D. J. Varon, A. Ramier, M. Strupler, and E. Tarrant. The GHGSat-D imaging spectrometer. *Atmospheric Measurement Techniques*, 14(3):2127–2140, 2021. doi: 10.5194/amt-14-2127-2021. URL <https://amt.copernicus.org/articles/14/2127/2021/>.
- E. N. Koffi and P. Bergamaschi. Evaluation of Copernicus Atmosphere Monitoring Service methane products. *Joint Research Centre: Ispra, Italy*, 2018.
- T. Lauvaux, C. Giron, M. Mazzolini, A. d’Aspremont, R. Duren, D. Cusworth, D. Shindell, and P. Ciais. Global assessment of oil and gas methane ultra-emitters. *Science*, 375(6580):557–561, 2022. doi: 10.1126/science.abj4351. URL <https://www.science.org/doi/abs/10.1126/science.abj4351>.
- A. Lorente, T. Borsdorff, A. Butz, O. Hasekamp, J. aan de Brugh, A. Schneider, L. Wu, F. Hase, R. Kivi, D. Wunch, D. F. Pollard, K. Shiomi, N. M. Deutscher, V. A. Velazco, C. M. Roehl, P. O. Wennberg, T. Warneke, and J. Landgraf. Methane retrieved from TROPOMI: improvement of the data product and validation of the first 2 years of measurements. *Atmospheric Measurement Techniques*, 14(1):665–684, 2021. doi: 10.5194/amt-14-665-2021. URL <https://amt.copernicus.org/articles/14/665/2021/>.
- A. Lorente, T. Borsdorff, M. C. Martinez-Velarte, and J. Landgraf. Accounting for surface reflectance spectral features in TROPOMI methane retrievals. *Atmospheric Measurement Techniques Discussions*, 2022:1–15, 2022. doi: 10.5194/amt-2022-255. URL <https://amt.copernicus.org/preprints/amt-2022-255/>.
- D. R. Lyon, D. Zavala-Araiza, R. A. Alvarez, R. Harriss, V. Palacios, X. Lan, R. Talbot, T. Lavoie, P. Shepson, T. I. Yacovitch, S. C. Herndon, A. J. Marchese, D. Zimmerle, A. L. Robinson, and S. P. Hamburg. Constructing a Spatially Resolved Methane Emission Inventory for the Barnett Shale Region. *Environmental Science & Technology*, 49(13):8147–8157, 2015. doi: 10.1021/es506359c. URL <https://doi.org/10.1021/es506359c>. PMID: 26148553.

- J. D. Maasackers, D. J. Jacob, M. P. Sulprizio, T. R. Scarpelli, H. Nesser, J.-X. Sheng, Y. Zhang, M. Hersher, A. A. Bloom, K. W. Bowman, J. R. Worden, G. Janssens-Maenhout, and R. J. Parker. Global distribution of methane emissions, emission trends, and OH concentrations and trends inferred from an inversion of GOSAT satellite data for 2010–2015. *Atmospheric Chemistry and Physics*, 19(11):7859–7881, 2019. doi: 10.5194/acp-19-7859-2019. URL <https://acp.copernicus.org/articles/19/7859/2019/>.
- J. D. Maasackers, M. Omara, R. Gautam, A. Lorente, S. Pandey, P. Tol, T. Borsdorff, S. Houweling, and I. Aben. Reconstructing and quantifying methane emissions from the full duration of a 38-day natural gas well blowout using space-based observations. *Remote Sensing of Environment*, 270:112755, 2022. ISSN 0034-4257. doi: <https://doi.org/10.1016/j.rse.2021.112755>. URL <https://www.sciencedirect.com/science/article/pii/S0034425721004752>.
- B. McWilliams, G. Sgaravatti, and G. Zachmann. European natural gas imports, bruegel datasets, 2021. URL <https://www.bruegel.org/dataset/european-natural-gas-imports>. last acces: 20 Jan 2023.
- National Centers for Environmental Prediction, National Weather Service, NOAA, U.S. Department of Commerce. Ncep fnl operational model global tropospheric analyses, continuing from july 1999, 2000. URL <https://doi.org/10.5065/D6M043C6>.
- I. B. Ocko, V. Naik, and D. Paynter. Rapid and reliable assessment of methane impacts on climate. *Atmospheric Chemistry and Physics*, 18(21):15555–15568, 2018. doi: 10.5194/acp-18-15555-2018. URL <https://acp.copernicus.org/articles/18/15555/2018/>.
- M. Omara, D. Zavala-Araiza, D. R. Lyon, B. Hmiel, K. A. Roberts, and S. P. Hamburg. Methane emissions from US low production oil and natural gas well sites. *Nature Communications*, 13(1), 2022. doi: 10.1038/s41467-022-29709-3.
- S. Pandey, R. Gautam, S. Houweling, H. D. van der Gon, P. Sadavarte, T. Borsdorff, O. Hasekamp, J. Landgraf, P. Tol, T. van Kempen, R. Hoogeveen, R. van Hees, S. P. Hamburg, J. D. Maasackers, and I. Aben. Satellite observations reveal extreme methane leakage from a natural gas well blowout. *Proceedings of the National Academy of Sciences*, 116(52):26376–26381, 2019. doi: 10.1073/pnas.1908712116. URL <https://www.pnas.org/doi/abs/10.1073/pnas.1908712116>.
- S. Pandey, M. van Nistelrooij, J. D. Maasackers, P. Sutar, S. Houweling, D. J. Varon, P. Tol, D. Gains, J. Worden, and I. Aben. Daily detection and quantification of methane leaks using Sentinel-3: a tiered satellite observation approach with sentinel-2 and sentinel-5p, 2022.
- J. G. Powers, J. B. Klemp, W. C. Skamarock, C. A. Davis, J. Dudhia, D. O. Gill, J. L. Coen, D. J. Gochis, R. Ahmadov, S. E. Peckham, G. A. Grell, J. Michalakes, S. Trahan, S. G. Benjamin, C. R. Alexander, G. J. Dimego, W. Wang, C. S. Schwartz, G. S. Romine, Z. Liu, C. Snyder, F. Chen, M. J. Barlage, W. Yu, and M. G. Duda. The Weather Research and Forecasting model: Overview, system efforts, and future directions. *Bulletin of the American Meteorological Society*, 98(8):1717–1737, 2017.
- Z. Qu, D. J. Jacob, L. Shen, X. Lu, Y. Zhang, T. R. Scarpelli, H. Nesser, M. P. Sulprizio, J. D. Maasackers, A. A. Bloom, J. R. Worden, R. J. Parker, and A. L. Delgado. Global distribution of methane emissions: a comparative inverse analysis of observations from the TROPOMI and GOSAT satellite instruments. *Atmospheric Chemistry and Physics*, 21(18):14159–14175, 2021. doi: 10.5194/acp-21-14159-2021. URL <https://acp.copernicus.org/articles/21/14159/2021/>.
- Rystad Ucube. Aggregated oil and gas production data, 2022. URL <https://www.rystadenergy.com/>. last acces: 28 Dec 2022.
- E. Sánchez-García, J. Gorroño, I. Irakulis-Loitxate, D. J. Varon, and L. Guanter. Mapping methane plumes at very high spatial resolution with the worldview-3 satellite. *Atmospheric Measurement Techniques*, 15(6):1657–1674, 2022. doi: 10.5194/amt-15-1657-2022. URL <https://amt.copernicus.org/articles/15/1657/2022/>.

- M. Saunio, A. R. Stavert, B. Poulter, P. Bousquet, J. G. Canadell, R. B. Jackson, P. A. Raymond, E. J. Dlugokencky, S. Houweling, P. K. Patra, P. Ciais, V. K. Arora, D. Bastviken, P. Bergamaschi, D. R. Blake, G. Brailsford, L. Bruhwiler, K. M. Carlson, M. Carrol, S. Castaldi, N. Chandra, C. Crevoisier, P. M. Crill, K. Covey, C. L. Curry, G. Etiope, C. Frankenberg, N. Gedney, M. I. Hegglin, L. Höglund-Isaksson, G. Hugelius, M. Ishizawa, A. Ito, G. Janssens-Maenhout, K. M. Jensen, F. Joos, T. Kleinen, P. B. Krummel, R. L. Langenfelds, G. G. Laruelle, L. Liu, T. Machida, S. Maksyutov, K. C. McDonald, J. McNorton, P. A. Miller, J. R. Melton, I. Morino, J. Müller, F. Murguía-Flores, V. Naik, Y. Niwa, S. Noce, S. O’Doherty, R. J. Parker, C. Peng, S. Peng, G. P. Peters, C. Prigent, R. Prinn, M. Ramonet, P. Regnier, W. J. Riley, J. A. Rosentreter, A. Segers, I. J. Simpson, H. Shi, S. J. Smith, L. P. Steele, B. F. Thornton, H. Tian, Y. Tohjima, F. N. Tubiello, A. Tsuruta, N. Viovy, A. Voulgarakis, T. S. Weber, M. van Weele, G. R. van der Werf, R. F. Weiss, D. Worthy, D. Wunch, Y. Yin, Y. Yoshida, W. Zhang, Z. Zhang, Y. Zhao, B. Zheng, Q. Zhu, Q. Zhu, and Q. Zhuang. The global methane budget 2000–2017. *Earth System Science Data*, 12(3):1561–1623, 2020. doi: 10.5194/essd-12-1561-2020. URL <https://essd.copernicus.org/articles/12/1561/2020/>.
- T. R. Scarpelli, D. J. Jacob, S. Grossman, X. Lu, Z. Qu, M. P. Sulprizio, Y. Zhang, F. Reuland, D. Gordon, and J. R. Worden. Updated Global Fuel Exploitation Inventory (GFEI) for methane emissions from the oil, gas, and coal sectors: evaluation with inversions of atmospheric methane observations. *Atmospheric Chemistry and Physics*, 22(5):3235–3249, 2022. doi: 10.5194/acp-22-3235-2022. URL <https://acp.copernicus.org/articles/22/3235/2022/>.
- O. Schneising, M. Buchwitz, M. Reuter, S. Vanselow, H. Bovensmann, and J. P. Burrows. Remote sensing of methane leakage from natural gas and petroleum systems revisited. *Atmospheric Chemistry and Physics*, 20(15):9169–9182, 2020. doi: 10.5194/acp-20-9169-2020. URL <https://acp.copernicus.org/articles/20/9169/2020/>.
- B. J. Schuit, J. D. Maasackers, P. Bijl, G. Mahapatra, A.-W. Van den Berg, S. Pandey, A. Lorente, T. Borsdorff, S. Houweling, D. J. Varon, J. McKeever, D. Jervis, M. Girard, I. Irakulis-Loitxate, J. Gorroño, L. Guanter, D. H. Cusworth, and I. Aben. Automated detection and monitoring of methane super-emitters using satellite data. *Atmospheric Chemistry and Physics Discussions*, 2023:1–47, 2023. doi: 10.5194/acp-2022-862. URL <https://acp.copernicus.org/preprints/acp-2022-862/>.
- D. J. Varon, D. J. Jacob, J. McKeever, D. Jervis, B. O. A. Durak, Y. Xia, and Y. Huang. Quantifying methane point sources from fine-scale satellite observations of atmospheric methane plumes. *Atmospheric Measurement Techniques*, 11(10):5673–5686, 2018. doi: 10.5194/amt-11-5673-2018. URL <https://amt.copernicus.org/articles/11/5673/2018/>.
- D. J. Varon, J. McKeever, D. Jervis, J. D. Maasackers, S. Pandey, S. Houweling, I. Aben, T. Scarpelli, and D. J. Jacob. Satellite discovery of anomalously large methane point sources from oil/gas production. *Geophysical Research Letters*, 46(22):13507–13516, 2019. doi: <https://doi.org/10.1029/2019GL083798>.
- D. J. Varon, D. Jervis, J. McKeever, I. Spence, D. Gains, and D. J. Jacob. High-frequency monitoring of anomalous methane point sources with multispectral Sentinel-2 satellite observations. *Atmospheric Measurement Techniques*, 14(4):2771–2785, 2021. doi: 10.5194/amt-14-2771-2021. URL <https://amt.copernicus.org/articles/14/2771/2021/>.
- D. J. Varon, D. J. Jacob, B. Hmiel, R. Gautam, D. R. Lyon, M. Omara, M. Sulprizio, L. Shen, D. Pendergrass, H. Nesser, Z. Qu, Z. R. Barkley, N. L. Miles, S. J. Richardson, K. J. Davis, S. Pandey, X. Lu, A. Lorente, T. Borsdorff, J. D. Maasackers, and I. Aben. Continuous weekly monitoring of methane emissions from the Permian Basin by inversion of TROPOMI satellite observations. *Atmospheric Chemistry and Physics Discussions*, 2022:1–26, 2022. doi: 10.5194/acp-2022-749. URL <https://acp.copernicus.org/preprints/acp-2022-749/>.
- J. Veefkind, I. Aben, K. McMullan, H. Förster, J. de Vries, G. Otter, J. Claas, H. Eskes, J. de Haan, Q. Kleipool, M. van Weele, O. Hasekamp, R. Hoogeveen, J. Landgraf, R. Snel, P. Tol, P. Ingmann,

- R. Voors, B. Kruizinga, R. Vink, H. Visser, and P. Levelt. TROPOMI on the ESA Sentinel-5 Precursor: A GMES mission for global observations of the atmospheric composition for climate, air quality and ozone layer applications. *Remote Sensing of Environment*, 120:70–83, 2012. ISSN 0034-4257. doi: <https://doi.org/10.1016/j.rse.2011.09.027>. URL <https://www.sciencedirect.com/science/article/pii/S0034425712000661>. The Sentinel Missions - New Opportunities for Science.
- L. M. Western, A. E. Ramsden, A. L. Ganesan, H. Boesch, R. J. Parker, T. R. Scarpelli, R. L. Tunnicliffe, and M. Rigby. Estimates of North African Methane Emissions from 2010 to 2017 Using GOSAT Observations. *Environmental Science & Technology Letters*, 8(8):626–632, 2021. doi: 10.1021/acs.estlett.1c00327.
- J. R. Worden, D. H. Cusworth, Z. Qu, Y. Yin, Y. Zhang, A. A. Bloom, S. Ma, B. K. Byrne, T. Scarpelli, J. D. Maasackers, D. Crisp, R. Duren, and D. J. Jacob. The 2019 methane budget and uncertainties at 1° resolution and each country through Bayesian integration of GOSAT total column methane data and a priori inventory estimates. *Atmospheric Chemistry and Physics*, 22(10):6811–6841, 2022. doi: 10.5194/acp-22-6811-2022. URL <https://acp.copernicus.org/articles/22/6811/2022/>.
- D. Zavala-Araiza, D. Lyon, R. A. Alvarez, V. Palacios, R. Harriss, X. Lan, R. Talbot, and S. P. Hamburg. Toward a Functional Definition of Methane Super-Emitters: Application to Natural Gas Production Sites. *Environmental Science & Technology*, 49(13):8167–8174, 2015. doi: 10.1021/acs.est.5b00133.

Supplement to “Assessing the relative importance of methane super-emitters and diffuse area sources in quantifying total emissions for oil and gas production areas in Algeria”

S. Naus^{1,*}, J. D. Maasakkers¹, R. Gautam², M. Omara², R. Stikker¹, A. K. Veenstra¹, B. Nathan¹, I. Irakulis-Loitxate^{3,4}, L. Guanter^{2,3}, S. Pandey^{1,5}, M. Girard⁶, A. Lorente-Delgado^{1,2}, T. Borsdorff¹, and I. Aben¹

¹SRON Netherlands Institute for Space Research, Leiden, Netherlands

²Environmental Defense Fund, Washington, DC 20009, USA

³Research Institute of Water and Environmental Engineering (IIAMA), Universitat Politècnica de València (UPV), Valencia 46022, Spain

³International Methane Emission Observatory, United Nations Environment Program, Paris, France

⁵Jet Propulsion Laboratory, California Institute of Technology, Pasadena, CA, US

⁶GHGSat Inc, Montréal, Canada

*Corresponding author: Stijn Naus (s.naus@sron.nl)

June 17, 2023

S1 Observation System Simulation Experiment (OSSE)

Here we discuss the results from the Observational System Simulation Experiment (OSSE), which provides a complementary perspective on the uncertainties in the inversion in addition to the sensitivity ensemble that is used for the final uncertainty estimates. In the OSSE, we used one of the five WRF simulations (which each use different planetary boundary layer (PBL) schemes; see Table S1) as truth, and used the other four simulations in the optimization to estimate emissions, in the same way as we do in our reference inversion using the best-matching of the four simulations for each individual day. For the OSSE, we need to set the true emission variations that are used to generate synthetic observations and the prior emission variations. We show here results where we choose the true emission variations as Gaussian variations with a standard deviation of 50%, i.e. the same as the prior uncertainty. The prior we choose as flat, with both point and diffuse sources at 13 t/hr, which is representative for the average situation in Hassi Messaoud. In the main OSSE, we use the same mean emissions for the prior and the truth, but we also show results when the prior and true emissions have a different mean. For the OSSE, we need to choose which PBL scheme to use as truth, but we find that the results are largely insensitive to this choice, and we show here results only for the OSSE where PBL1 is used as truth. We only show the OSSE analysis for Hassi Messaoud, as the conclusions for Hassi R'Mel are similar.

Fig. S1 shows the prior, posterior and true emission timeseries. It is clear that not all true emission variations are retrieved. The difference between posterior and true emissions decreases when we average over longer timescales (Fig. S2), and it depends on the difference between prior and posterior. Typically, we find that estimates of daily emissions have an error of 6-8 t/hr, which decreases to 3-4 t/hr on weekly to monthly timescales. This error increases if the difference between the prior and the truth increases, but since our daily

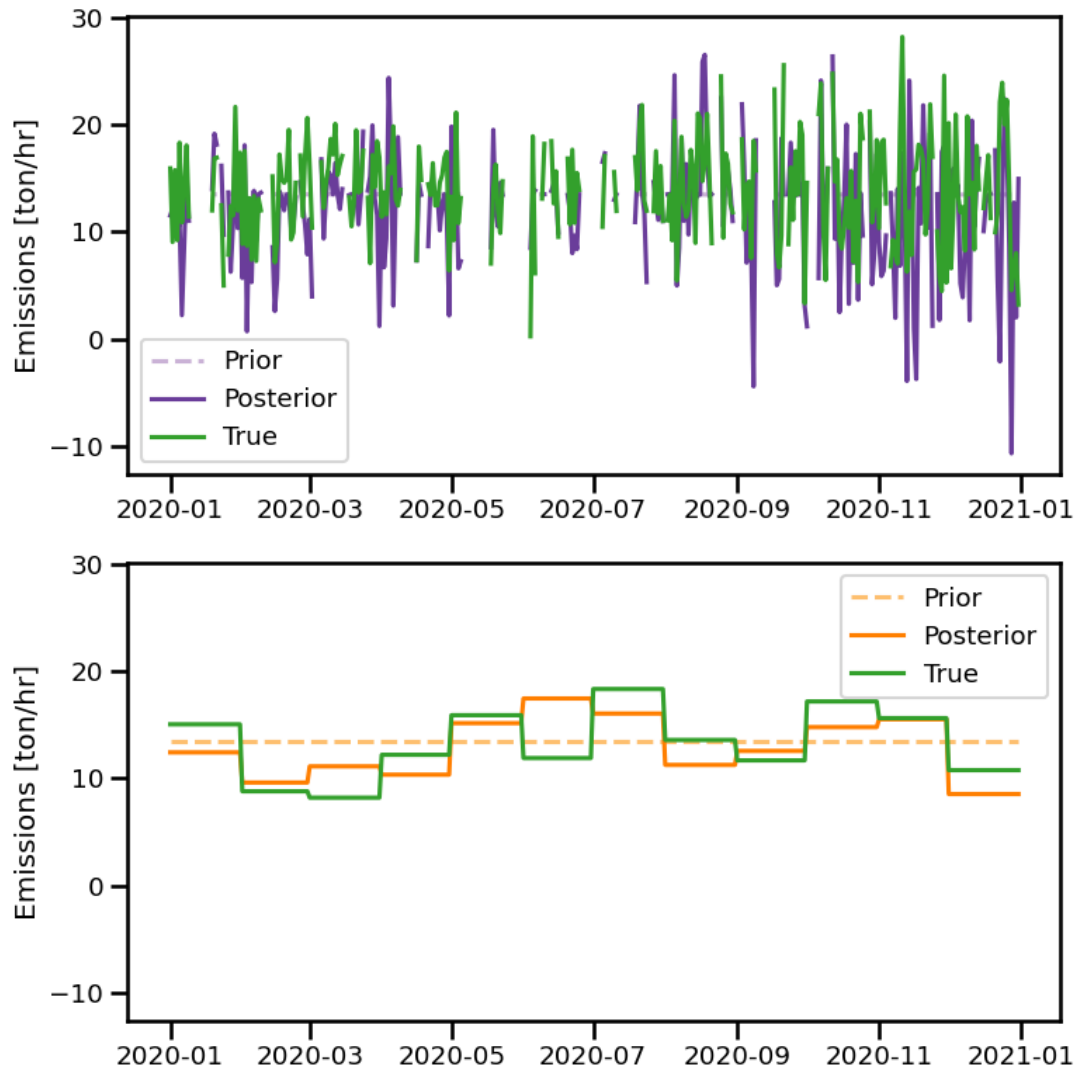


Figure S1: Prior, posterior and true timeseries for the point (top) and diffuse sources (bottom), as used for and retrieved in the OSSE.

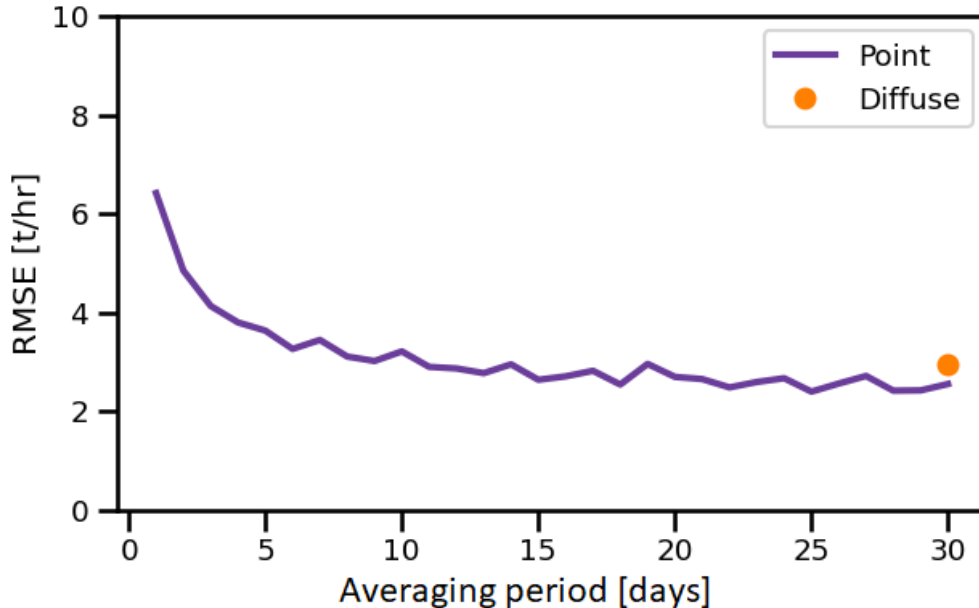


Figure S2: Root mean square error (RMSE) between posterior and true emissions as a function of the timescale over which emissions are averaged. The line shows the results for the daily point source emissions, while the orange dot gives the value for the diffuse sources (that are only optimized on a monthly basis).

emissions are based on the Sentinel-2 analysis, we consider that these are somewhat close to the truth. Since these uncertainty estimates are largely in line with the results from the sensitivity ensemble, we consider them roughly representative, although the OSSE analysis does not include all transport uncertainties, since each of the five simulations is driven by the same meteorological data.

In addition to the random error, we find a systematic underestimate of emissions in the reference OSSE (Fig. S3). In the OSSE where the prior and the truth use the same mean emissions, point sources are underestimated by approximately 20%, while the diffuse emissions are estimated correctly. The underestimate is strongest on days where the mismatch between the true plume and the plume used for optimization is larger. We can identify these cases by the low correlation between the true and the posterior observations when we exclude observational noise. However, this relation cannot be used to correct for the underestimate, since it is obscured when we introduce observational noise. We consider that since the point source plumes are sharper, they are harder to capture in simulations than more diffuse plumes, resulting in the observed underestimate. The underestimate depends strongly on the difference between the prior and the truth: if the prior is much lower, the underestimate grows, and if it is higher it largely disappears (Fig. S3). This is a consequence of the weight of the prior in the cost function, which increases when larger adjustments are needed. Again, we consider that our prior for point sources in the analysis of the main manuscript is likely reasonably close to the truth, since it is constructed from the Sentinel-2 analysis.

While our OSSE is a useful tool to assess uncertainties of the inverse system, there are limitations. Importantly, all five WRF simulations were driven by the same meteorological data (NCEP), which means that while the simulated plumes vary significantly (e.g. Fig. 2 in main text), they are generally more similar than the simulated versus TROPOMI-observed plumes. Additionally, we have explored the effect of Gaussian noise in the synthetic TROPOMI data on the quality of the emission estimate, but TROPOMI errors are not purely Gaussian and can have large-scale (bias) patterns that can result in significant uncertainties in the emission estimate. Both limitations likely result in an underestimate of the uncertainty. However, the

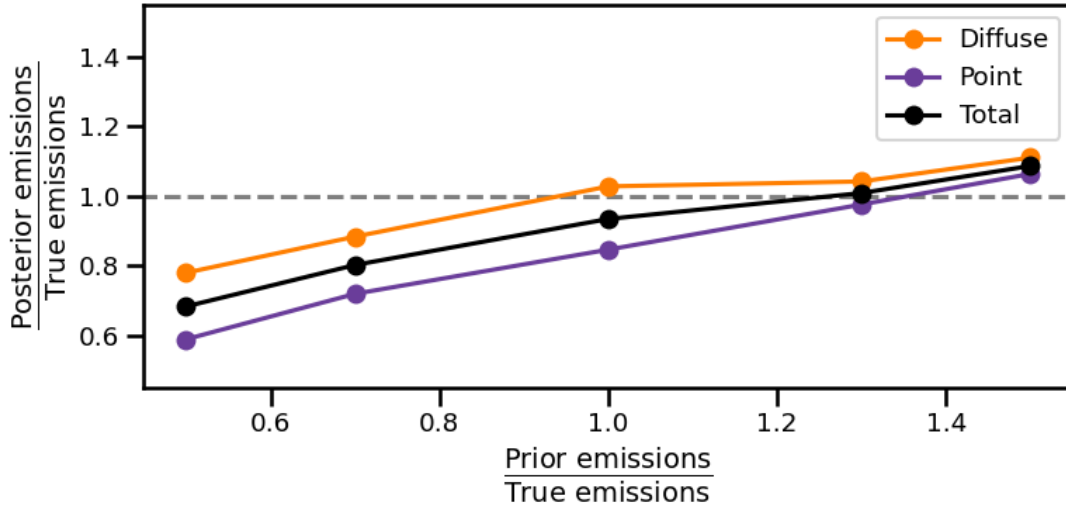


Figure S3: Ratios between prior and true emissions (x-axis) and posterior and true emissions (y-axis), for five different OSSE’s that each have a different scaling of the prior (i.e., the x-axis).

general findings (e.g., the underestimated point source contribution) are applicable to our inversions.

S2 Details on Sentinel-2 analysis

We have analysed Sentinel-2 methane data over Hassi R’Mel and Hassi Messaoud, and detected one source in Hassi R’Mel and ten in Hassi Messaoud (see Table S4 and Fig. S4). The aggregate results and important conclusions are presented in the main manuscript. Here, we provide some additional details.

Fig. S4 shows visual imagery of each source location, which we use to identify the facility type per source (given in Table S4). Sources emit with a range of frequencies, from one plume detection for M07 to 102 (90.3% of days with good data) for M03a. It is possible that on days with no plume detection, sources still emit, but below the Sentinel-2 detection limit (see also Section S3). The source rates also vary between locations: M06 has the highest average emissions, but plumes are detected only on three days. Afterwards, frequent flaring is visible in Sentinel-2 at M06, which ends in May 2020. M08 (also in Varon et al. [2021]) emits on the high end for semi-continuous sources (8.4 t/hr compared to e.g., 3.9 ton/hour for M03a). M08 stops emitting after 8 Aug 2020. Similar to M06, after M08 stops emitting Sentinel-2 shows flaring at this location, with the last flare visible in Sentinel-2 on 26 Aug 2020. Additionally, on 7 Sentinel-2 overpasses in 2020 flaring is visible at M07. Further details are provided in Table S4.

Our emissions for M08 compare well (on average lower by 0.4 t/hr) to those reported in Varon et al. [2021] (left panel in Fig S4). The remaining differences between our estimates likely come from differences in the retrieval (e.g., our use of a ten-day median reference day), differences in the plume masking approach and the wind dataset that is used for the effective wind speed calculation (here: ERA-5; in Varon et al. [2021]: GEOS-FP). Pandey et al. [2022] report a Sentinel-2 based emission rate for 4 Jan 2020 at M06 of 21 ± 6 t/hr, calculated with cross-sectional flux method, which is consistent with our estimate of 29 ± 15 t/hr.

All Hassi Messaoud sources produce plumes that are isolated enough for individual IME quantification. However, the Hassi R’Mel source R01 is located near several flares towards the west and south-west (visible in middle panel of Fig. S4) that are turned on for most of 2020. On days where the plume is transported over the flares, we can still identify that R01 is emitting, but the IME quantification becomes unreliable due to flare-induced saturation of the SWIR band overlapping the plume. To allow for point source emissions in the posterior on these days, we set the source rate to the average source rate on days where we can get a

reliable quantification (red markers in left panel of Fig. S4).

S3 GHGSat detections near M06 in Hassi Messaoud

To better understand the Sentinel-2 plume data, we use five observations by GHGSat-C1 over Hassi Messaoud. GHGSat-C1 is a dedicated methane satellite instrument retrieving plume images at ~ 25 -m resolution for $\sim 10 \times 15$ km² spatial domains. Emissions are calculated using the IME method as described in Maasackers et al. [2022]. The GHGSat constellation has been reported to have a detection limit of ~ 100 kg hr⁻¹ [ESA, 2022] and detected an emission event of ~ 200 kg hr⁻¹ in a blind controlled release study [Sherwin et al., 2022].

In each of the five GHGSat observations (Fig. S5) we detect plumes from an inactive flare at (31.843, 6.143) near the M06 site with emission rates of 0.4-1.2 t hr⁻¹. Emissions from the same source are detected on 6 other days by Sentinel-2 with emission rates of 2.5-5.1 t hr⁻¹. On November 7 and 14, Sentinel-2 provides coverage over the site but the emission plumes are not detectable above the noise, illustrating that there are large point source emissions beyond those detected by Sentinel-2.

PBL scheme	Full name
1	Yonsei University Scheme (YSU) [Hong et al., 2006]
2	Mellor–Yamada–Janjic Scheme (MYJ) [Janjić, 1994]
3	NCEP Global Forecast System Scheme (GFS) [Hong and Pan, 1996]
4	Quasi–normal Scale Elimination Scheme (QNSE) [Sukoriansky et al., 2005]
5	Mellor–Yamada Nakanishi Niino Level 2.5 (MYNN2) [Nakanishi and Niino, 2006]

Table S1: Planetary boundary layer (PBL) schemes used for the five different WRF-Chem simulations.

	Point source emissions [Tg/yr]	Diffuse emissions [Tg/yr]	Total emissions [Tg/yr]
Hassi R'Mel			
Prior	0.06 [0.03-0.09]	0.33 [0.17-0.50]	0.39 [0.19-0.58]
Posterior	0.04 [0.02-0.06]	0.12 [0.08-0.18]	0.16 [0.11-0.22]
Hassi Messaoud			
Prior	0.13 [0.06-0.19]	0.12 [0.06-0.18]	0.25 [0.12-0.37]
Posterior	0.11 [0.06-0.15]	0.11 [0.06-0.17]	0.22 [0.13-0.28]

Table S2: Annual total emissions per investigated domain for the super-emitters and the diffuse area emissions, with ranges indicating the full range of the sensitivity ensemble (see Table 1 in main manuscript).

	Point source emissions [Tg/yr]	Diffuse emissions [Tg/yr]	Total emissions [Tg/yr]
Hassi R'Mel			
Prior	0.00	0.33	0.33
Posterior	0.00	0.18	0.18
Hassi Messaoud			
Prior	0.00	0.12	0.12
Posterior	0.00	0.21	0.21

Table S3: Annual total emissions for one inversion per investigated domain in which the TROPOMI data was coarsened to 1.0° resolution, only diffuse emissions are included, and in which we optimize the CAMS background monthly. This inversion is intended to represent conventional inversions that cover larger areas with generally lower spatial resolution. This result falls within the uncertainty ensemble of the reference inversions (see Table S2)

Name	Lat [°]	Lon [°]	Plume count	Plume %	Q_{av} [t/hr]	Source type
R01	32.8414	3.2428	34	72.3	5.26	Pit flare.
M01	31.7570	6.1689	5	4.2	4.43	Ground flare.
M02	31.6166	5.9671	5	4.2	6.71	Ground flare.
M03a	31.7777	5.9951	102	90.3	3.91	Ground flare.
M03b	31.7687	6.0003	47	43.9	3.86	Ground flare.
M04	31.7333	5.9678	28	25.2	3.31	Ground flare.
M05	31.7563	5.9425	14	13.1	2.19	Ground flare.
M06	31.8639	6.1730	3	2.5	32.54	Production well.
M07	31.1637	5.9652	1	0.8	8.23	Ground flare.
M08	31.6585	5.9053	71	60.7	8.39	Ground flare.
M09	31.7458	5.9027	61	59.2	3.38	Ground flare.

Table S4: Source locations found in the Sentinel-2 analysis. For each source we provide the coordinates, the number of plume detections in 2020 (Plume count), the percentage of days with good Sentinel-2 data (e.g., no clouds) that have plumes (Plume %), the average IME-calculated emission rate on days with a plume detection (Q_{av}), and the identification of the source based on visual imagery (see Fig. 3 and Fig S4).

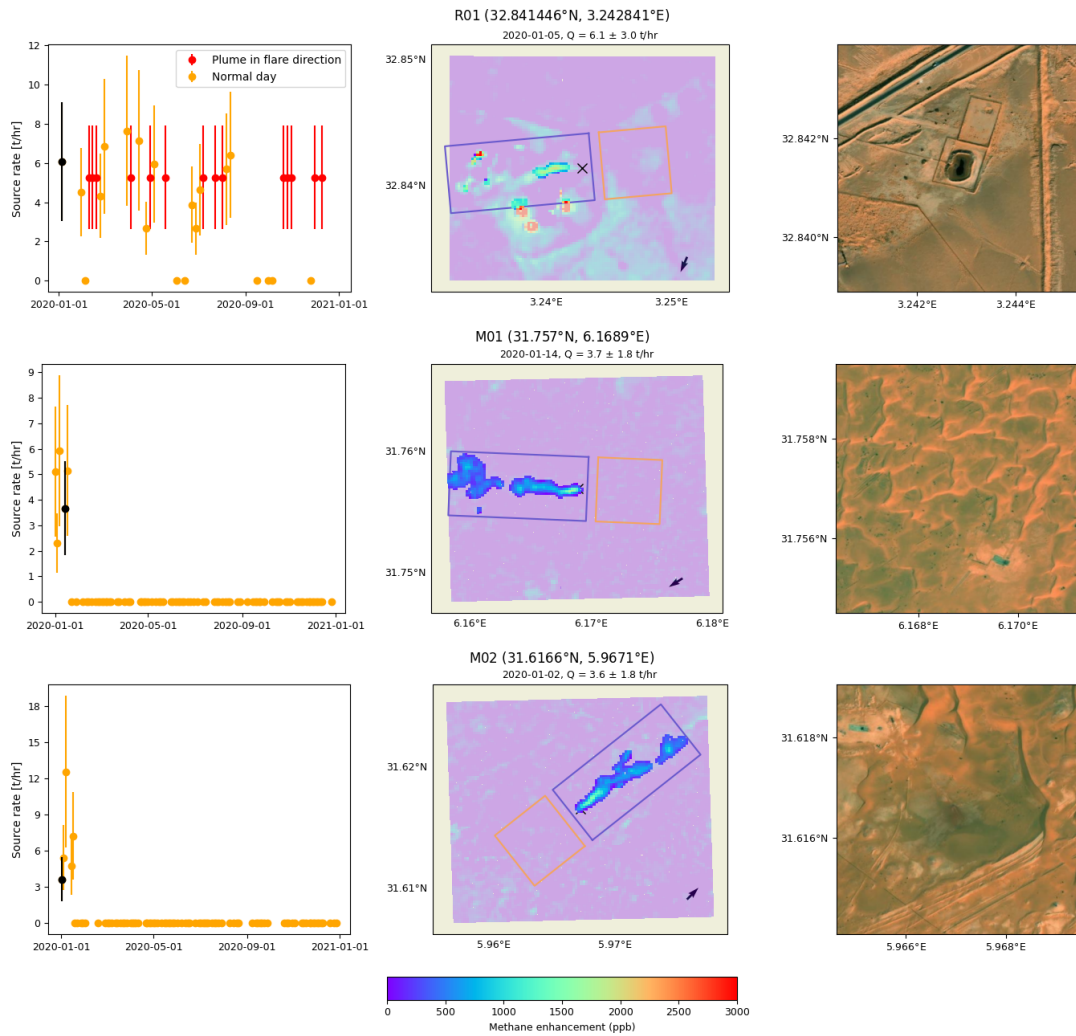


Figure S4: Sentinel-2 detections and IME-calculated emission timeseries per site. The left column shows the emission timeseries per source location (orange, with black indicating the day shown in the middle panel), literature estimates (purple; M06: Pandey et al. [2022]; M08: Varon et al. [2021]), and red markers show for R01 days on which a visible plume overlaps with flares. For these days we take the 2020 averaged source rate, since the IME quantification is unreliable. Uncertainty margins indicate the 50% 1-SD that is used in the inversion. The middle column shows the IME plume quantification for one day (marked with black in left column), with the source location marked with x, the plume box marked in blue, the background box in orange, and the plume mask as bright colors. The arrow shows the 10-m ERA-5 wind direction. Source location, date and the estimated source rate are given at the top of the figure. The right column shows the visual Bing imagery (©Vexcel Imaging, 2023) that is used to identify the source.

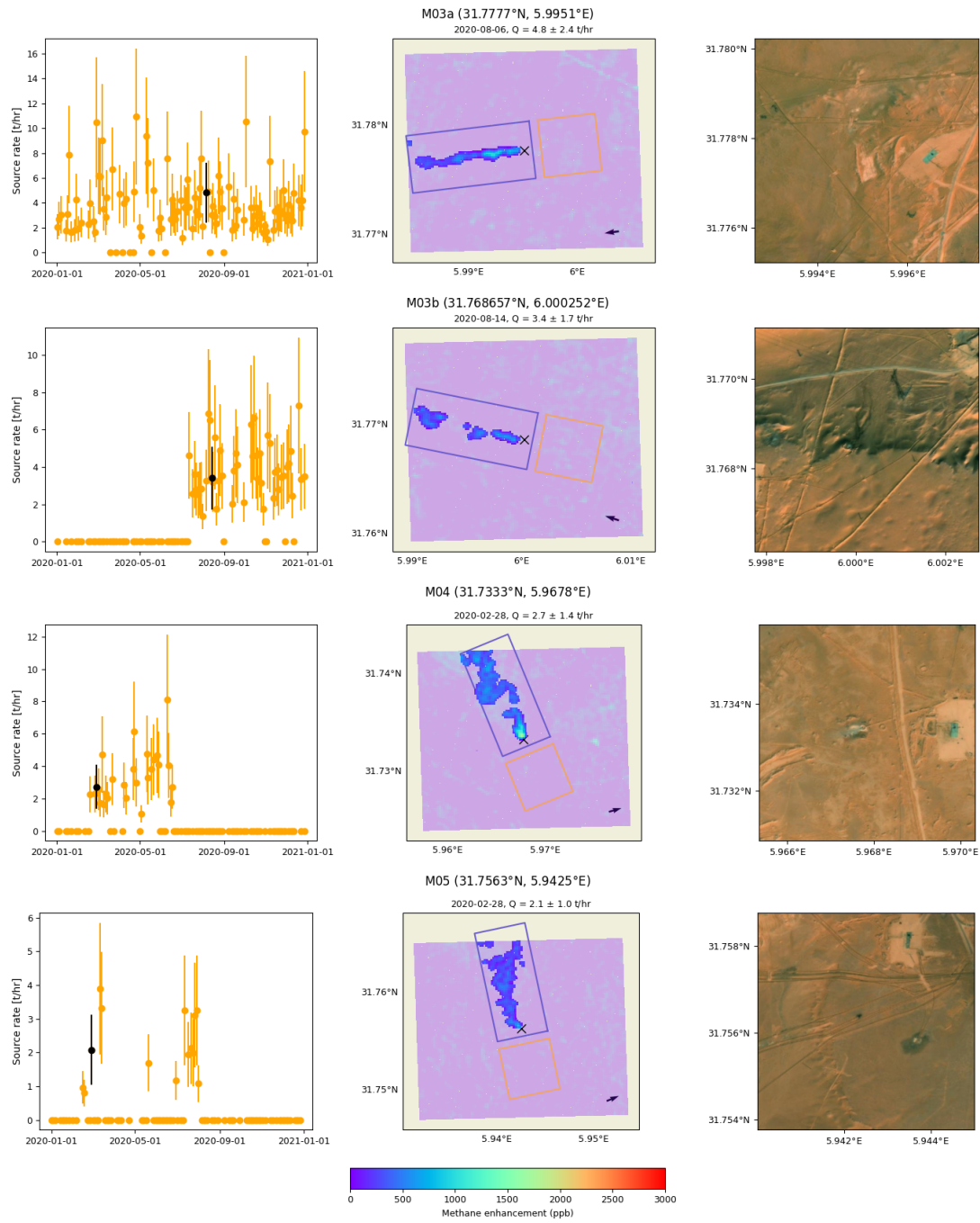


Figure S4: Continued.

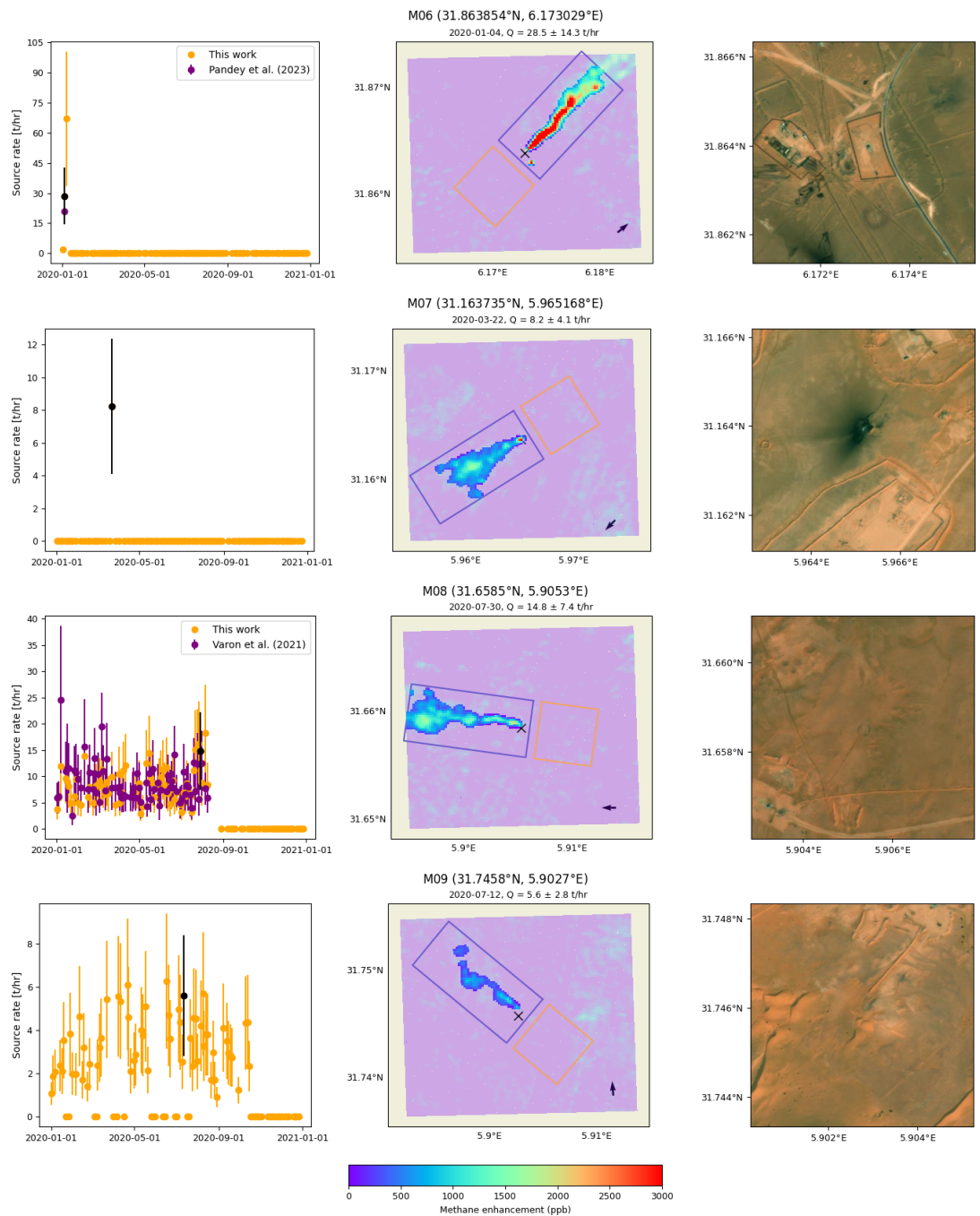


Figure S4: Continued.

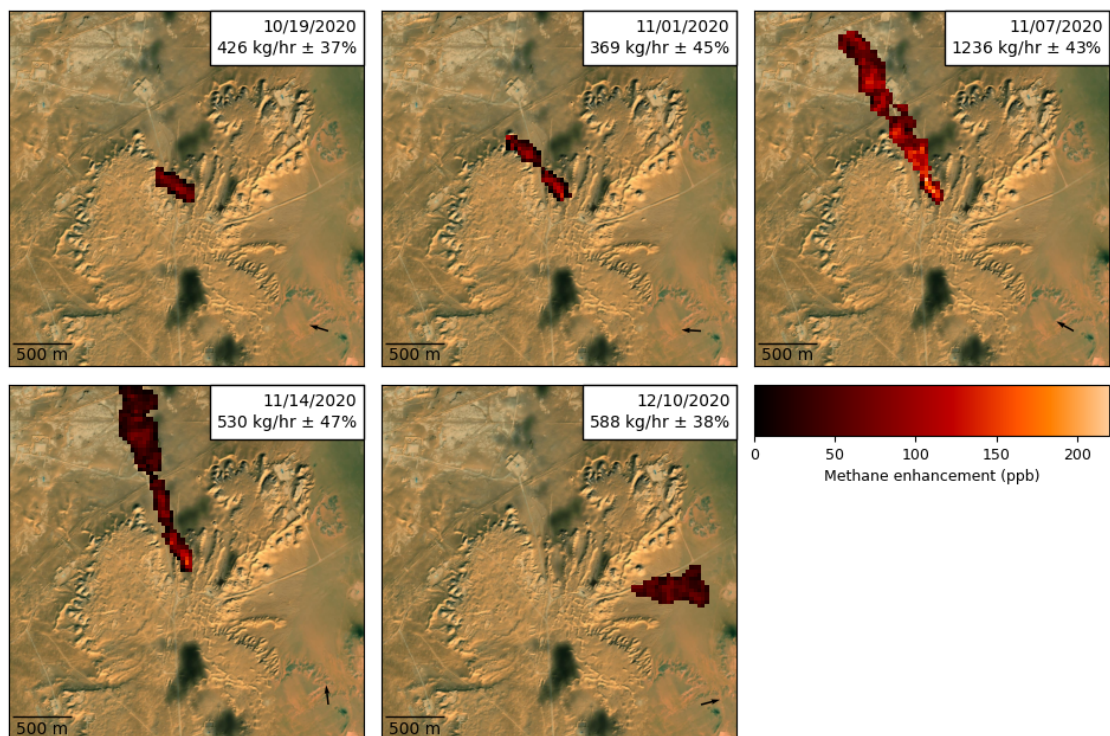


Figure S5: Plumes observed near the M06 location by GHGSat-C1. Emission estimates are based on the IME method as described in Maasackers et al. [2022]. Emissions come from an inactive flare on all days except for December 10, when emissions originate more eastward. Background imagery taken from ESRI World Imagery [ESRI et al., 2022]. Black arrows in the bottom right indicate the GEOS-FP wind direction.

References

- G. ESA. GHGSat mission overview, 2022. URL <https://earth.esa.int/eogateway/missions/ghgsat>.
- ESRI, Maxar, E. Geographics, and the GIS User Community. ESRI world imagery, 2022. URL https://services.arcgis.com/ArcGIS/rest/services/World_Imagery/MapServer.
- S.-Y. Hong and H.-L. Pan. Nonlocal boundary layer vertical diffusion in a medium-range forecast model. *Monthly Weather Review*, 124(10):2322 – 2339, 1996. doi: 10.1175/1520-0493(1996)124<2322:NBLVDI>2.0.CO;2. URL https://journals.ametsoc.org/view/journals/mwre/124/10/1520-0493_1996_124_2322_nblvdi_2_0_co_2.xml.
- S.-Y. Hong, Y. Noh, and J. Dudhia. A new vertical diffusion package with an explicit treatment of entrainment processes. *Monthly weather review*, 134(9):2318–2341, 2006.
- Z. I. Janjić. The step-mountain eta coordinate model: Further developments of the convection, viscous sublayer, and turbulence closure schemes. *Monthly Weather Review*, 122(5):927 – 945, 1994. doi: 10.1175/1520-0493(1994)122<0927:TSMECM>2.0.CO;2. URL https://journals.ametsoc.org/view/journals/mwre/122/5/1520-0493_1994_122_0927_tsmeccm_2_0_co_2.xml.
- J. D. Maasackers, M. Omara, R. Gautam, A. Lorente, S. Pandey, P. Tol, T. Borsdorff, S. Houweling, and I. Aben. Reconstructing and quantifying methane emissions from the full duration of a 38-day natural gas well blowout using space-based observations. *Remote Sensing of Environment*, 270:112755, 2022. ISSN 0034-4257. doi: <https://doi.org/10.1016/j.rse.2021.112755>. URL <https://www.sciencedirect.com/science/article/pii/S0034425721004752>.
- M. Nakanishi and H. Niino. An improved Mellor–Yamada level-3 model: Its numerical stability and application to a regional prediction of advection fog. *Boundary-Layer Meteorology*, 119:397–407, 2006.
- S. Pandey, M. van Nistelrooij, J. D. Maasackers, P. Sutar, S. Houweling, D. J. Varon, P. Tol, D. Gains, J. Worden, and I. Aben. Daily detection and quantification of methane leaks using Sentinel-3: a tiered satellite observation approach with sentinel-2 and sentinel-5p, 2022.
- E. D. Sherwin, J. S. Rutherford, Y. Chen, S. Aminfard, E. A. Kort, R. B. Jackson, and A. R. Brandt. Single-blind validation of space-based point-source methane emissions detection and quantification. 2022.
- S. Sukoriansky, B. Galperin, and V. Perov. Application of a new spectral theory of stably stratified turbulence to the atmospheric boundary layer over sea ice. *Boundary-layer meteorology*, 117:231–257, 2005.
- D. J. Varon, D. Jervis, J. McKeever, I. Spence, D. Gains, and D. J. Jacob. High-frequency monitoring of anomalous methane point sources with multispectral Sentinel-2 satellite observations. *Atmospheric Measurement Techniques*, 14(4):2771–2785, 2021. doi: 10.5194/amt-14-2771-2021. URL <https://amt.copernicus.org/articles/14/2771/2021/>.